



boundary sliding, which dominate at fine grain sizes—can operate over prolonged timescales. During grain-size-sensitive creep, viscosity decreases as grain sizes are reduced. Thus, self-softening feedbacks and long-lived weakening are thought to arise from coupled grain size reduction and phase mixing. Indeed, two-phase “damage” theory has been used to successfully model the initiation and persistence of Earth-like plate tectonics (Bercovici & Ricard, 2014). Still, there remains continued discussion over the precise mechanisms responsible for grain-scale phase mixing, and the relevant time- or strain-scales over which mixing occurs.

Experimental and field-based models for phase mixing can be separated into two broad categories—mechanical and chemical—each containing several proposed mechanisms. Mechanical phase mixing can occur by dynamic recrystallization coupled with grain switching during grain boundary sliding (Farla et al., 2013; Linckens et al., 2014), the sequential formation, attenuation (stretching), and disaggregation of compositional layering (Cross & Skemer, 2017) and/or the nucleation of well-mixed grains at interphase triple junctions (Bercovici & Skemer, 2017). Chemical phase mixing, on the other hand, may involve the formation of a well-mixed metamorphic reaction product (Dijkstra et al., 2002; Kenkmann & Dresen, 2002; Kruse & Stünitz, 1999; Marti et al., 2018; Newman et al., 1999), the exchange of chemical species between phases (Tasaka et al., 2017), and/or the precipitation of phases into dilational sites (Kenkmann & Dresen, 2002; Kilian et al., 2011; Platt, 2015) including creep cavities formed via grain boundary sliding (Czertowicz et al., 2016; Lopez-Sanchez & Llana-Fúnez, 2018; Menegon et al., 2015; Précigout et al., 2017; Viegas et al., 2016), Zener-Stroh cracking (Gilgannon et al., 2017), or dynamic recrystallization (Gilgannon et al., 2020). Chemical phase mixing mechanisms may be extremely efficient, since well-mixed reaction products can form even in the absence of deformation. However, these reactions generally require fluid flux (to enable mass transfer) or changes in thermodynamic state (to drive metamorphic reactions). Furthermore, creep cavitation is thought to become increasingly difficult as confining pressure,  $P$ , exceeds differential stress,  $\sigma$  (i.e., above the Goetze criterion; Kohlstedt et al., 1995), although strain incompatibilities and stress concentrations can promote local microcracking and void generation even in the middle to lower crust where confining pressures match or exceed bulk differential stresses ( $P \geq \sigma$ ) (Gilgannon et al., 2017; Précigout et al., 2019).

To explore the mechanisms and timescales required for phase mixing under deep-lithosphere ( $P \gg \sigma$ ) conditions—and in the absence of chemical phase mixing—Cross and Skemer (2017) examined the microstructural evolution of calcite-anhydrite composites deformed to large shear strains ( $\gamma > 50$ ). In their experiments, confining pressures (1.5 GPa) were maintained well in excess of differential stresses ( $<0.3$  GPa). Phase mixing progressed by the geometric shearing and elongation of polycrystalline monophase domains to form compositional layering (Figures 1a–1f). At large shear strains ( $\gamma \gg 10$ ), compositional layers became severely attenuated and eventually disaggregated to form a near-perfectly mixed aggregate (Figures 1f–1g). Calcite grain sizes in well-mixed regions collapsed onto a linear trend—subparallel with the calcite recrystallized grain size piezometer but lying within the diffusion creep regime (e.g., Bercovici & Ricard, 2016)—indicating significant weakening. More recently, a similar style of geometric mixing was reported in high-strain torsion experiments on copper-silver and copper-aluminum multilayer stacks (Pouryazdan et al., 2017) and olivine-ferropericlase mixtures (Wiesman et al., 2018). Notably, Wiesman et al. (2018) measured a secondary stage of mechanical weakening beginning at  $\gamma = 10$ , coinciding with the onset of widespread grain-scale mixing. However, none of these experimental studies directly explored the influence of viscosity contrast on phase mixing mechanisms and timescales. In natural systems, on the other hand, viscosity contrasts are common due to the differing mechanical properties of individual phases, which vary as a function of deformation conditions (e.g., temperature, stress, and water content).

To examine the effects of viscosity contrast on phase mixing dynamics, we present a series of high-strain experiments on nonisoviscous calcite-fluorite composites. Through microstructural and rheological analyses of the deformed samples, we identify the mechanisms for phase mixing and assess the role of viscosity contrast in modifying phase mixing timescales.

## 2. Methods

### 2.1. Starting Material

Two different calcite-fluorite composites were synthesized. A 50-50 vol.% mixture (hereafter referred to as  $\text{Ca}_{50}\text{-Fl}_{50}$ ) was produced by gently stirring together fine (1–5  $\mu\text{m}$ ) reagent-grade powders of  $\text{CaCO}_3$



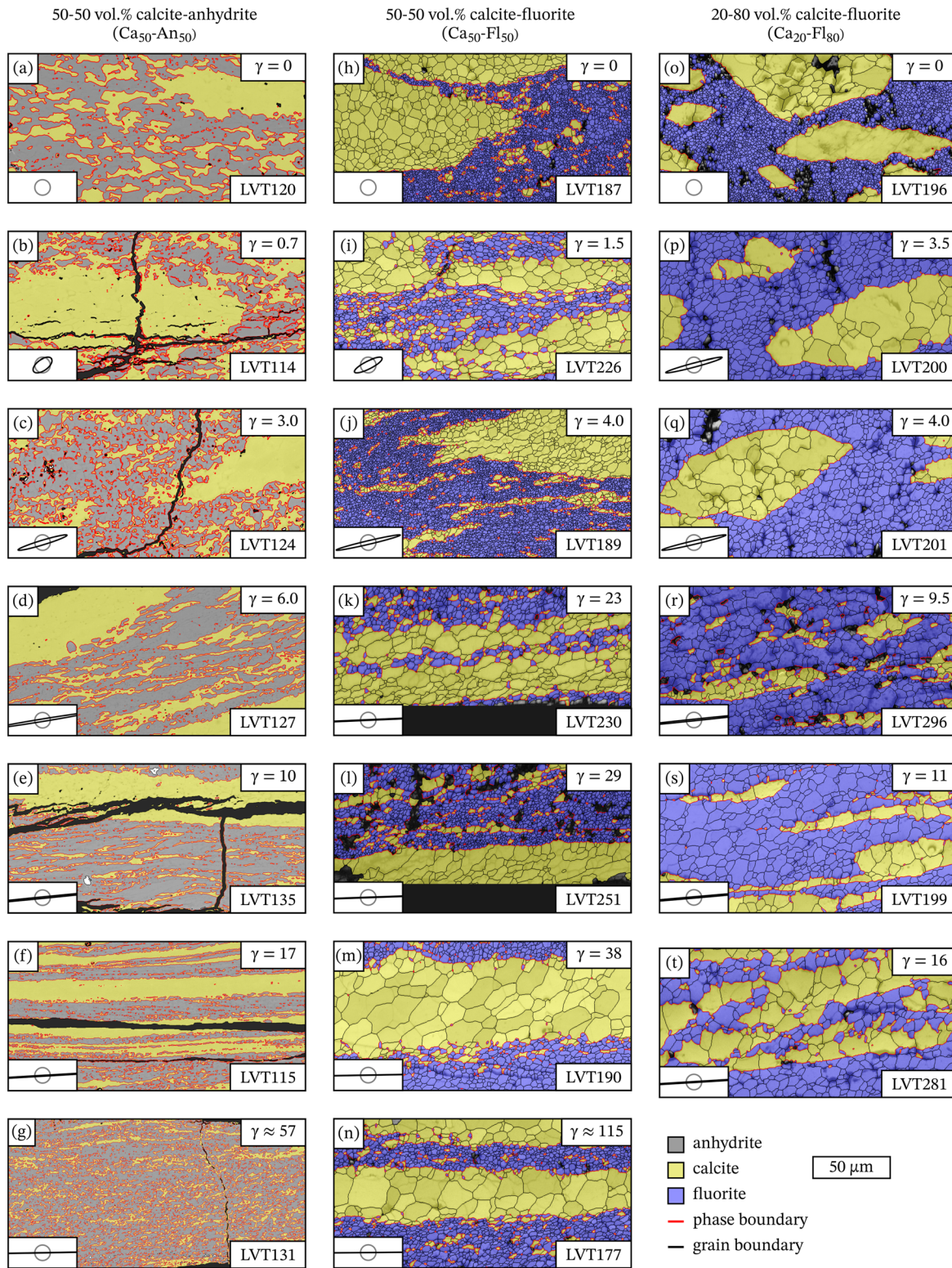


**Figure 1.** Phase maps of (a–g) 50-50 vol.% calcite-anhydrite (from Cross & Skemer, 2017, for reference), (h–n) 50-50 vol.% calcite-fluorite, and (o–t) 20-80 vol.% calcite-fluorite composites. The calcite-anhydrite maps are false-colored BSE images, with calcite (yellow) and anhydrite (gray) separated by their backscatter intensity. Black regions are decompression cracks and holes formed by grains plucking during polishing. The calcite-fluorite maps are EBSD phase maps (calcite in yellow; fluorite in blue) plotted on top of band contrast (EBSD pattern quality) maps. Grain boundaries ( $\geq 10^\circ$  misorientation) are shown in black; interphase boundaries are shown in red. The finite strain ellipse for each experiment is shown in the lower left of each map. Dextral shear sense (top-to-the-right). Strain increases downward.

**Table 1**  
Summary of Experimental Runs

Run no.	Angular shear (°) <sup>a</sup>	Shear strain, $\gamma$	Duration, $t$ (hr)	Bulk shear strain rate, $\gamma_{\text{bulk}}$ (s <sup>-1</sup> )	Anvil rotation, $\omega$ (°)	Final sample thickness, $l$ (mm)	Target shear strain, $\gamma_t$ <sup>b</sup>	IGSN <sup>c</sup>
<i>50 vol.% calcite, 50 vol.% fluorite (Ca<sub>50</sub>-Fl<sub>50</sub>)</i>								
LVT187	0.00	0.0	0.50	0.0	0.0	0.21	0.00	IESPM002R
LVT226	42.5	1.5	74.0	$5.6 \times 10^{-6}$	534.8	0.16	122	IESPM003T
LVT189	76.0	4.0	2.00	$5.6 \times 10^{-4}$	15.2	0.18	3.10	IESPM002S
LVT230	87.5	23	30.0	$2.1 \times 10^{-4}$	227.0	0.10	83.2	IESPM003X
LVT251	88.0	29	14.2	$5.7 \times 10^{-4}$	107.8	0.09	43.9	IESPM004I
LVT190	88.5	38	44.0	$2.4 \times 10^{-4}$	333.2	0.18	67.8	IESPM002T
LVT177	89.5	~115	66.0	$4.8 \times 10^{-4}$	165.7	0.17	35.7	IESPM002H
<i>20 vol.% calcite, 80 vol.% fluorite (Ca<sub>20</sub>-Fl<sub>80</sub>)</i>								
LVT196	0.00	0.0	0.50	0.0	0.0	0.16	0.00	IESPM002Z
LVT200	74.0	3.5	22.0	$4.4 \times 10^{-5}$	166.9	0.20	30.6	IESPM0033
LVT201	76.0	4.0	4.40	$2.5 \times 10^{-4}$	32.7	0.19	6.31	IESPM0034
LVT296	84.0	9.5	84.0	$2.2 \times 10^{-5}$	620.0	0.23	98.8	IESPM005K
LVT199	85.0	11	66.0	$3.1 \times 10^{-5}$	494.0	0.13	139	IESPM0032
LVT281	86.5	16	19.0	$2.3 \times 10^{-4}$	145.5	0.20	26.7	IESPM0055

Note. All experiments are performed at 500°C and have a confining pressure of 0.75 GPa.

<sup>a</sup>Measured on sections cut tangential to the deformed sample disc. Uncertainty =  $\pm 0.5^\circ$ . <sup>b</sup>Calculated from Equation 1, assuming perfect coupling across sample-piston and piston-anvil interfaces. <sup>c</sup>International Geo Sample Number unique identifier.

(calcite) and CaF<sub>2</sub> (fluorite). Pellets of this poorly mixed material were isostatically hot-pressed at 220°C and 30 MPa for 20 min in a Buehler Simplimet 4000 mounting press. This procedure produced a starting microstructure very similar to that of the calcite-anhydrite (Ca<sub>50</sub>-An<sub>50</sub>) material studied by Cross and Skemer (2017), with large polycrystalline domains of calcite embedded in a matrix of fluorite and calcite (compare Figures 1a and 1h).

To eliminate any grain-scale mixing of calcite and fluorite in the starting material and to produce a material with initially smooth phase boundaries, we also synthesized a 20 vol.% calcite, 80 vol.% fluorite composite (hereafter referred to as Ca<sub>20</sub>-Fl<sub>80</sub>) by embedding single crystals of calcite in the same reagent-grade CaF<sub>2</sub> powder used for the Ca<sub>50</sub>-Fl<sub>50</sub> mixture. Calcite grains were produced by crushing and sieving Carrara marble to a particle size fraction of 53–106  $\mu\text{m}$ , before settling the powder several times through deionized water to remove any remaining fine grains ( $< 53 \mu\text{m}$ ). This powder was dried in a vacuum oven overnight at 110°C, mixed with fluorite, and isostatically hot-pressed using the same procedure outlined above. The resulting material contains relatively large individual grains of calcite (50–100  $\mu\text{m}$ ) suspended in a matrix of fluorite, with sharp boundaries between the two phases (Figure 1o). Note that some of the calcite grains underwent static recrystallization during hot-pressing and the ramp to experimental run conditions, driven by preexisting defects or dislocations introduced during mechanical synthesis (i.e., crushing).

Half-cylinders (2.1 mm in diameter) were cut from the hot-pressed pellets using a Roland MDC-40A CNC milling machine and sectioned into half-discs of 0.5 mm thickness. For each experiment, two half-discs were put together to form a disc-shaped sample (4.2 mm in diameter, 0.5 mm thick), with gold sputter-coated on the joining surface to act as a passive strain marker. To control the water content in each experiment, samples were kept in a vacuum oven at 110°C for 12 hr before each experimental run.

## 2.2. Experimental Procedure

In total, we performed six deformation experiments on the Ca<sub>50</sub>-Fl<sub>50</sub> composite, and five deformation experiments on the Ca<sub>20</sub>-Fl<sub>80</sub> composite (Table 1). One additional experiment was performed on each material under nominally hydrostatic conditions to obtain reference specimen microstructures prior to any imposed deformation. All experiments were performed in the solid-medium Large Volume Torsion (LVT) apparatus (Washington University in St. Louis) at 0.75 GPa confining pressure and 500°C. To make the cell assembly more stable at high P-T conditions, experiments were performed without a thermocouple. Instead, furnace power was held constant, and temperature was estimated from power-temperature calibration curves generated during separate experiments. Further details on the LVT and cell assembly are given in Cross and Skemer (2017) and supporting information Figure S1, respectively.



At the start of each experiment, pressure and furnace power were increased in a stepwise manner to run conditions, over a period of around 3 hr. Samples were held at these conditions for 30 min to an hour, enabling samples to fully densify before the rotational actuator was turned on to begin deformation. Samples were deformed in a torsional geometry at a constant twist rate, yielding shear strain rates between  $5 \times 10^{-6}$  and  $5 \times 10^{-4} \text{ s}^{-1}$  at the outer radius of the sample. Torque was measured between the gear train and torsional actuator; however, due to friction and mechanical noise, we do not report stress measurements. At the end of each experiment, electrical power to the graphite furnace was turned off, quenching the sample to below  $300^\circ\text{C}$  within a few seconds. Confining pressure was reduced over several hours to minimize the formation of decompression cracks.

Sample shear strains ( $\gamma$ ) from 0 to 50–115 were determined by measuring the passive rotation of the gold strain markers. Significant uncertainties in resolving shear strains greater than  $\gamma = 50$  arise from the difficulty in precisely determining strain marker rotations greater than  $89^\circ$ ; for example, strain marker rotations of  $89^\circ$  and  $89.5^\circ$  correspond to shear strains of 57 and 115, respectively. The targeted shear strain at the outer edge of the sample,  $\gamma_t$ , is given by the rotation of the bottom anvil relative to the (fixed) top anvil, assuming no slip occurs at the anvil-piston and piston-sample interfaces:

$$\gamma_t = \frac{\pi d \omega}{360 l} \quad (1)$$

where  $d$  is sample diameter,  $l$  is sample height, and  $\omega$  is the imposed anvil rotation (Paterson & Olgaard, 2000). Here,  $l$  is taken as the final sample height, since thinning occurred during pressurization. However, undeformed and deformed samples had similar sample heights (Table 1), indicating that little thinning occurred during deformation. Experiments where the measured shear strain,  $\gamma$ , exceeds the target shear strain,  $\gamma_t$ , represent strain localization into a layer thinner than the sample itself.

### 2.3. Microstructural Analysis

Tangential sections (i.e., sections containing the shear direction and shear plane normal) were cut across the radius of each sample and polished for microstructural analysis. Samples were polished with silicon carbide grit paper (to 1,200 grit), followed by diamond paste (to  $1 \mu\text{m}$ ), and, finally, colloidal silica solution. A 3.5 nm-thick carbon coat was applied to mitigate sample charging in the scanning electron microscope.

Detailed microstructural mapping of each sample was performed using electron backscatter diffraction (EBSD). Samples were imaged under high-vacuum conditions in a JEOL 7001-LVF or ThermoFischer Quattro field emission scanning electron microscope at 20 kV accelerating voltage. EBSD patterns were collected using an Oxford Instruments Symmetry EBSD detector, with  $2 \times 2$  pattern binning and three-frame averaging. These settings enabled pattern collection and indexing at a frequency of 70–100 Hz with high indexing rates ( $>90\%$  in regions devoid of decompression cracks and holes). Maps were collected by rastering the electron beam across each sample, with a step-size of  $0.25 \mu\text{m}$ .

EBSD data were cleaned using the EBSDinterp toolbox for MATLAB (Pearce, 2015). In the first pass of cleaning, nonindexed pixels were filled if they had three or more neighboring pixels of a common orientation. During this step, band contrast masking (after Prior et al., 2009) was employed to ensure that only regions of high pattern quality were filled. In the second cleaning pass, nonindexed pixels with six or more common neighbors were filled without band contrast masking. Wild-spike pixels were also removed during the second pass. Thereafter, the cleaned EBSD data were analyzed using the MTEX toolbox for MATLAB (Bachmann et al., 2010). Grains were defined as regions surrounded by a critical misorientation of  $10^\circ$ , while grains containing fewer than four pixels were discarded, along with grains with less than 50% of their area comprised of indexed pixels (Cross et al., 2015).

## 3. Results

### 3.1. Textural Evolution

With increasing shear strain, calcite domains become sheared and elongated, forming ellipses that mimic the finite strain ellipse (e.g., Figures 1i–1k and 1p–1s). At shear strains as low as  $\gamma = 4$  in the  $\text{Ca}_{50}\text{Fl}_{50}$  composite (Figure 1j), thin calcite “monolayers”—that is, layers of only one grain’s thickness—begin to form. Conspicuous necking and rending of compositional layers can be seen at a shear strain of 11 in the  $\text{Ca}_{20}$ -

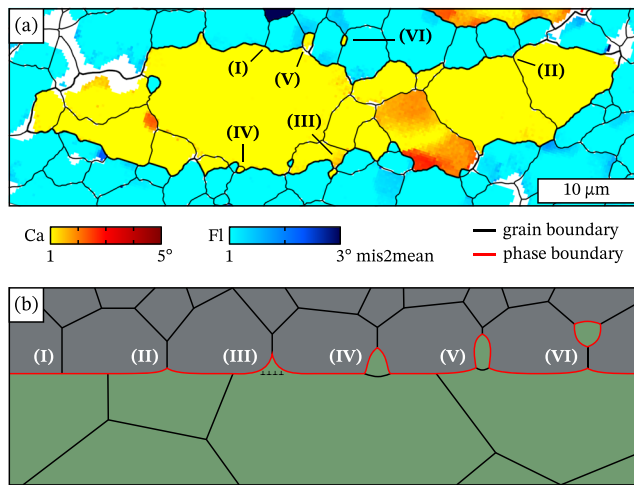


**Figure 2.** Local phase mixing along the margins of polycrystalline phase domains. (a) EBSD maps colored by the “mis2mean” of each pixel (i.e., the misorientation angle between each pixel and the mean orientation of the grain to which they belong). Maps are from sample LVT201: Ca<sub>20</sub>-Fl<sub>80</sub> composition, deformed to  $\gamma = 4$ . (b) A conceptual model for local grain-scale mixing, after Bercovici and Skemer (2017). As neighboring phases undergo recrystallization, triple junctions form in unstable configurations (stage I). To minimize their surface energy, triple junctions migrate toward favorable dihedral angles, drawing material into a “tooth” (stages II and III). This “tooth” becomes a new grain through subgrain rotation recrystallization (stages III and IV) and migrates into the opposing phase (stages IV and VI), resulting in local phase mixing. Microstructures suggestive of each stage in this process can be seen in (a).

Fl<sub>80</sub> sample, where fluorite-filled necks bisect calcite monolayers (e.g., Figure 1s). However, at shear strains equivalent to those required for complete phase mixing in the calcite-anhydrite experiments ( $\gamma \geq 50$ ; Figure 1g), thick polycrystalline calcite layers remain intact—without significant necking, buckling, or boudinaging—and phase mixing appears largely incomplete (Figures 1m–1n).

In addition to bulk phase mixing (or, rather, a lack thereof) via the formation and attenuation of compositional layers, we also observe local, grain-scale mixing along the margins of polycrystalline phase domains (Figure 2). Local mixing is highlighted by the “injection” of individual calcite grains into fluorite domains and vice versa (Figure 2a), forming a two-phase mantle surrounding large, polycrystalline phase domains (e.g., Figures 1m and 1n). This process is more conspicuous in the Ca<sub>20</sub>-Fl<sub>80</sub> samples (Figures 1p–1t), which had sharp interphase boundaries and no grain-scale mixing in the undeformed starting material (compare Figures 1h and 1o). However, even at very large strains ( $\gamma \gg 10$ ; Figures 1k–1n), mixing is limited to within one or two grain length scales ( $\sim 10 \mu\text{m}$ ) of phase domain margins.

### 3.2. Phase Boundary Density

To quantify the progression of phase mixing, we calculate the spatial density of phase boundaries,  $\delta = L/A$  (units:  $\mu\text{m}/\mu\text{m}^2$ ) as a function of strain, where  $L$  is the total length of phase boundary per unit area,  $A$ . As phase mixing progresses, interphase boundaries are generated, causing an increase in  $\delta$ . For a randomly interspersed mixture of two phases,  $\delta$  follows an inverse linear function of the grain size,  $d$ , of the least abundant (“minor”) phase—that is, when the minor phase is finer grained, there is a greater spatial density of phase boundaries:

$$\delta = \alpha d^{-1} \quad (2)$$

where  $\alpha$  is a constant that depends on the volume fraction of the minor phase. Using Monte Carlo simulations of random mixtures of equant grains, Cross and Skemer (2017) derived a value of  $\alpha = 0.925$  for a 50–50 vol.% two-phase composite—see their supplementary Figure S3. Thus, for a grain size of  $1 \mu\text{m}$  (the mean grain size of well-mixed grains in the calcite-anhydrite samples), phase boundary density should reach a maximum value of  $0.925 \mu\text{m}/\mu\text{m}^2$ . Indeed, Cross and Skemer (2017) reported a steady increase in  $\delta$  with increasing strain (Figure 3, gray circles), up to a maximum value of  $0.80 \mu\text{m}/\mu\text{m}^2$  ( $\pm 0.11 \mu\text{m}/\mu\text{m}^2$ ) at  $\gamma \approx 57$  where near-complete mixing was observed (Figure 1g).

As in the calcite-anhydrite experiments, calcite grains in the Ca<sub>50</sub>-Fl<sub>50</sub> samples evolve toward a mean grain size of  $1 \mu\text{m}$  in well-mixed regions; thus, the maximum expected value of  $\delta$  is  $0.925 \mu\text{m}/\mu\text{m}^2$ , as in Cross and Skemer (2017). However, while  $\delta$  increases modestly over low to intermediate strains (Figure 3, yellow squares), beyond  $\gamma \approx 20$  there is little change in  $\delta$ , which remains at a near-steady state value of  $0.34 \mu\text{m}/\mu\text{m}^2$ —less than half the value expected for a well-mixed composite. Note that some scatter in these values is a direct result of heterogeneity in the starting material: samples cored from well-mixed regions of the hot-pressed starting material have inherently higher phase boundary densities. Nevertheless, mixing appears markedly slower in the nonisoviscous calcite-fluorite samples.

### 3.3. Grain Size and Shape

In polyphase composites, grain boundary pinning by secondary phases inhibits grain coarsening (Evans et al., 2001; Smith, 1948), disrupting the dynamic competition between grain size reduction and grain growth and resulting in the suppression of grain size (Cross & Skemer, 2017; Hiraga et al., 2010; Linckens et al., 2015; Tasaka et al., 2017; Wiesman et al., 2018). To isolate the effects of grain boundary pinning during phase mixing, we divide grains into two populations: those that are poorly mixed (i.e., surrounded predominately by

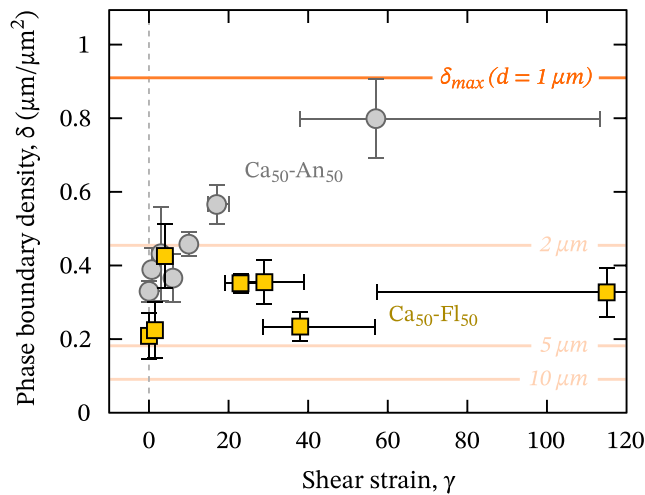


**Figure 3.** The spatial density of interphase boundaries,  $\delta$  ( $\mu\text{m}/\mu\text{m}^2$ ), as a function of shear strain, for 50-50 vol.% composites of calcite-anhydrite (gray circles; Cross & Skemer, 2017) and calcite-fluorite (yellow squares; this study). Phase boundary densities were measured from several BSE images of each sample (see Cross & Skemer, 2017, for details). Horizontal error bars represent the error in shear strain for  $\pm 0.5^\circ$  uncertainty in the angular shear of the passive strain marker. Vertical error bars give  $1\sigma$  errors in phase boundary density. Maximum values of  $\delta$  for randomly interspersed two-phase mixtures of 1, 2, 5, and 10  $\mu\text{m}$  grains are shown in orange. The limit corresponding to a 1  $\mu\text{m}$  grain size is most appropriate for both the calcite-anhydrite and calcite-fluorite samples, which evolve to a  $\sim 1 \mu\text{m}$  mean grain size in well-mixed regions.

grains of the same phase) and those that are well mixed (i.e., surrounded predominately by grains of the opposite phase). Following Cross and Skemer (2017), grain populations are subdivided according to their phase boundary fraction,  $P_{pb} = L_{pb}/L_{total}$ , where  $L_{total}$  is the total boundary length (i.e., perimeter) of a given grain, and  $L_{pb}$  is the length of that grain's perimeter composed of phase boundary. Here, we use  $P_{pb} < 0.25$  and  $P_{pb} > 0.75$  to define poorly-mixed and well-mixed grains, respectively. These constraints are tighter than those used by Cross and Skemer ( $P_{pb} < 0.5$  and  $P_{pb} > 0.5$ , respectively), to prevent cross-contamination of the two populations. In practice, however, the threshold values used to define poorly-mixed and well-mixed grains had no systematic or significant effect on our results.

In the calcite-anhydrite ( $\text{Ca}_{50}\text{-An}_{50}$ ) experiments, both the poorly mixed ( $P_{pb} < 0.5$ ) and well-mixed ( $P_{pb} > 0.5$ ) calcite grain populations underwent net grain size reduction. However, while the poorly-mixed grains converged with the calcite grain size paleowattmeter (as expected for a single-phase aggregate), well-mixed grains were suppressed below the paleowattmeter. In the calcite-fluorite ( $\text{Ca}_{50}\text{-Fl}_{50}$ ) samples presented here, however, we observe calcite grain size evolution that is markedly different. While well-mixed ( $P_{pb} > 0.75$ ) calcite grains maintain a small (1–3  $\mu\text{m}$ ) grain size throughout (Figure 4a, red points), poorly-mixed ( $P_{pb} < 0.25$ ) calcite grains undergo modest grain size reduction only over low to moderate shear strains ( $\gamma \leq 10$ ; Figure 4a, blue points). Grain size reduction is accom-

panied by the development of a strong shape preferred orientation (SPO) (Figure 4b), with ribbon grains forming with aspect ratios of up to 10 (Figure 1j). At larger strains, however, poorly-mixed calcite grains coarsen significantly, increasing to a maximum grain size of  $\sim 30 \mu\text{m}$  at  $\gamma > 50$  (Figures 1m and 1n). As calcite grains coarsen, their SPO weakens such that, at  $\gamma > 50$ , coarse calcite grains are nominally equant (i.e., aspect ratios  $\leq 1.5$ ; Figure 4b). In contrast, fluorite grains and well-mixed calcite grains remain equant across the full range of experimental strain. We also note, briefly, that poorly-mixed calcite grains of the  $\text{Ca}_{20}\text{-Fl}_{80}$  samples undergo continuous, modest grain size reduction, reaching similar grain sizes of  $\leq 30 \mu\text{m}$  at large strains, while maintaining equant shapes (Figures 1o–1t).

### 3.4. Crystallographic Preferred Orientation

Calcite CPO evolution in the  $\text{Ca}_{50}\text{-Fl}_{50}$  samples is similar to that observed in the  $\text{Ca}_{50}\text{-An}_{50}$  samples of Cross and Skemer (2017). Poorly-mixed calcite grains develop a reasonably strong  $(0001)\langle\bar{1}2\bar{1}0\rangle$  crystallographic alignment, whereas well-mixed calcite grains maintain a weak  $(0001)\langle\bar{1}2\bar{1}0\rangle$  fabric over the range of strains explored here. Fluorite pole figures (Figure 5) and inverse pole figures (Figure S3), on the other hand, are much weaker in all samples and display no apparent evolution with strain. Quantitative measures of CPO strength—the M-index (Skemer et al., 2005) and J-index (Bunge, 1982)—support these observations: poorly-mixed calcite grains have relatively strong CPOs ( $M \leq 0.2$ ;  $J \leq 10$ ), whereas fluorite grains ( $M = 0.00$ ;  $J \approx 1.00$ ) and well-mixed calcite grains ( $M \leq 0.04$ ;  $J \leq 5$ ) have weak or even uniform CPOs (Figures 5 and S3).

### 3.5. Intragranular Misorientations

During deformation, calcite grains of the  $\text{Ca}_{50}\text{-Fl}_{50}$  samples develop pronounced subgrain structures (Figures 6a–6g), reflected in the evolution of calcite misorientation distribution functions (MDFs). With increasing strain, calcite neighbor-pair misorientation angle distributions (yellow histograms, Figures 6h–6n) shift toward low angles ( $< 10^\circ$ ) relative to the uniform calcite MDF (black curve, Figures 6h–6n). At low to intermediate strains, intragranular misorientations in calcite are small and spatially diffuse, giving a misorientation distribution peak at  $\sim 2^\circ$  representing smooth lattice curvature (e.g., Figure 6j). At larger strains, however, intragranular misorientation gradients become sharper, producing



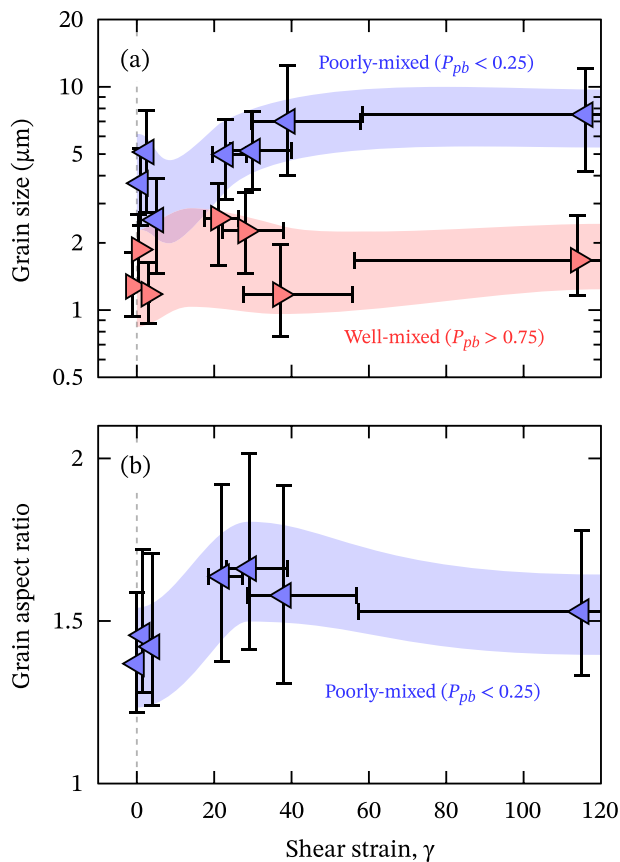


**Figure 4.** (a) Calcite grain size and (b) calcite grain aspect ratio as a function of shear strain. Calcite grains are separated into poorly-mixed and well-mixed populations based on their phase boundary fraction,  $P_{pb}$  (i.e., the fraction of their perimeter comprised of interphase boundary). Poorly-mixed grains (blue triangles) are defined as those with  $P_{pb} < 0.25$  (i.e.,  $<25\%$  of their perimeter comprised of phase boundary), while well-mixed grains (red triangles) are those with  $P_{pb} > 0.75$ . Only poorly-mixed calcite grain aspect ratios are plotted in (b), since well-mixed grains show no appreciable shape change. Data points show the median values of grain size and aspect ratio for a given sample. Horizontal error bars represent  $\pm 0.5^\circ$  uncertainty in angular shear of the passive strain marker, whereas vertical error bars represent the interquartile range. Shaded regions schematically show the evolution of grain size and aspect ratio with increasing strain.

an additional peak at  $10\text{--}20^\circ$  that corresponds to the development of sub-grain walls (e.g., Figure 6l). MDFs for the  $\text{Ca}_{20}\text{-Fl}_{80}$  samples show a similar evolution (Figure S4), although calcite grains initially have much higher intragranular misorientations due to dislocations introduced during sample synthesis (see section 2.1). In fluorite, on the other hand, intragranular misorientations are relatively scarce, and fluorite neighbor-pair misorientation angle distributions (blue histograms, Figures 6o–6u) largely conform to the uniform fluorite MDF (black curve, Figures 6o–6u).

## 4. Discussion

The nonisoviscous calcite-fluorite samples presented here exhibit both similarities and differences with the previously studied isoviscous calcite-anhydrite samples. As in the calcite-anhydrite experiments, sample textures evolve over long transient intervals (shear strains,  $\gamma \gg 10$ ) via the geometric shearing of monomineralic phase domains to form compositional layering (Figure 1). Bulk-scale phase mixing produces a monotonic increase in the spatial density of phase boundaries with increasing strain (Figure 3), while local, grain-scale mixing is also observed along the margins of polycrystalline phase domains (Figure 2). Well-mixed calcite grains are significantly smaller than poorly-mixed calcite grains (Figure 4a) and have markedly weaker CPOs (Figure 5). Unlike the calcite-anhydrite samples, however, complete phase mixing is not observed in the calcite-fluorite composites (over a similar range of strain—compare Figures 1g and 1n). Thick calcite layers are preserved to large shear strains ( $\gamma > 50$ ) and undergo significant grain coarsening with increasing strain (Figure 4a). In the following discussion, we examine these similarities and differences to explore the influence of viscosity contrast on phase mixing, namely, in terms of the strains required for mixing, and the processes by which mixing occurs. While the rheological behavior of calcite has been investigated extensively, little is known about the rheological behavior of fluorite. We must first, therefore, determine the viscosity contrast between calcite and fluorite. Unless stated otherwise, we focus our discussion on the  $\text{Ca}_{50}\text{-Fl}_{50}$  samples, for direct comparison with the  $\text{Ca}_{50}\text{-An}_{50}$  samples of Cross and Skemer (2017).

### 4.1. Deformation Mechanisms

To establish the relative viscosities of calcite and fluorite, it is useful to examine the primary mechanisms by which each phase deforms under the experimental conditions imposed here. To isolate any two-phase effects and determine the deformation behavior of the end-member

phases alone, we examine microstructures in only the poorly mixed regions (i.e., monomineralic and polycrystalline domains) of calcite and fluorite.

Poorly mixed regions of calcite and fluorite exhibit markedly different deformation microstructures. Calcite grains are larger ( $5\text{--}30\ \mu\text{m}$ ), have elongated grain shapes (particularly at intermediate strains), contain abundant intragranular misorientation substructures, and develop a well-defined CPO (Figures 4–6). Elongated grain shapes, strong CPOs, and intragranular misorientation substructures, in particular, are diagnostic of deformation accommodated by dislocation creep (e.g., White, 1976). Indeed, our microstructural observations closely resemble those made by other authors on calcite polycrystals deformed within the dislocation creep regime (e.g., Barnhoorn et al., 2004; Pieri et al., 2001). Fluorite grains, on the other hand, are small ( $<2\ \mu\text{m}$ ), equant, and randomly oriented, with little internal crystallographic distortion (Figures 4–6); in other words, lacking microstructures indicative of dislocation creep and, moreover, contrasting with observations made on other halide minerals deformed by dislocation creep (e.g., Pennock et al., 2005). Instead, such microstructures are commonly associated with superplastic flow (see Boullier & Gueguen, 1975),

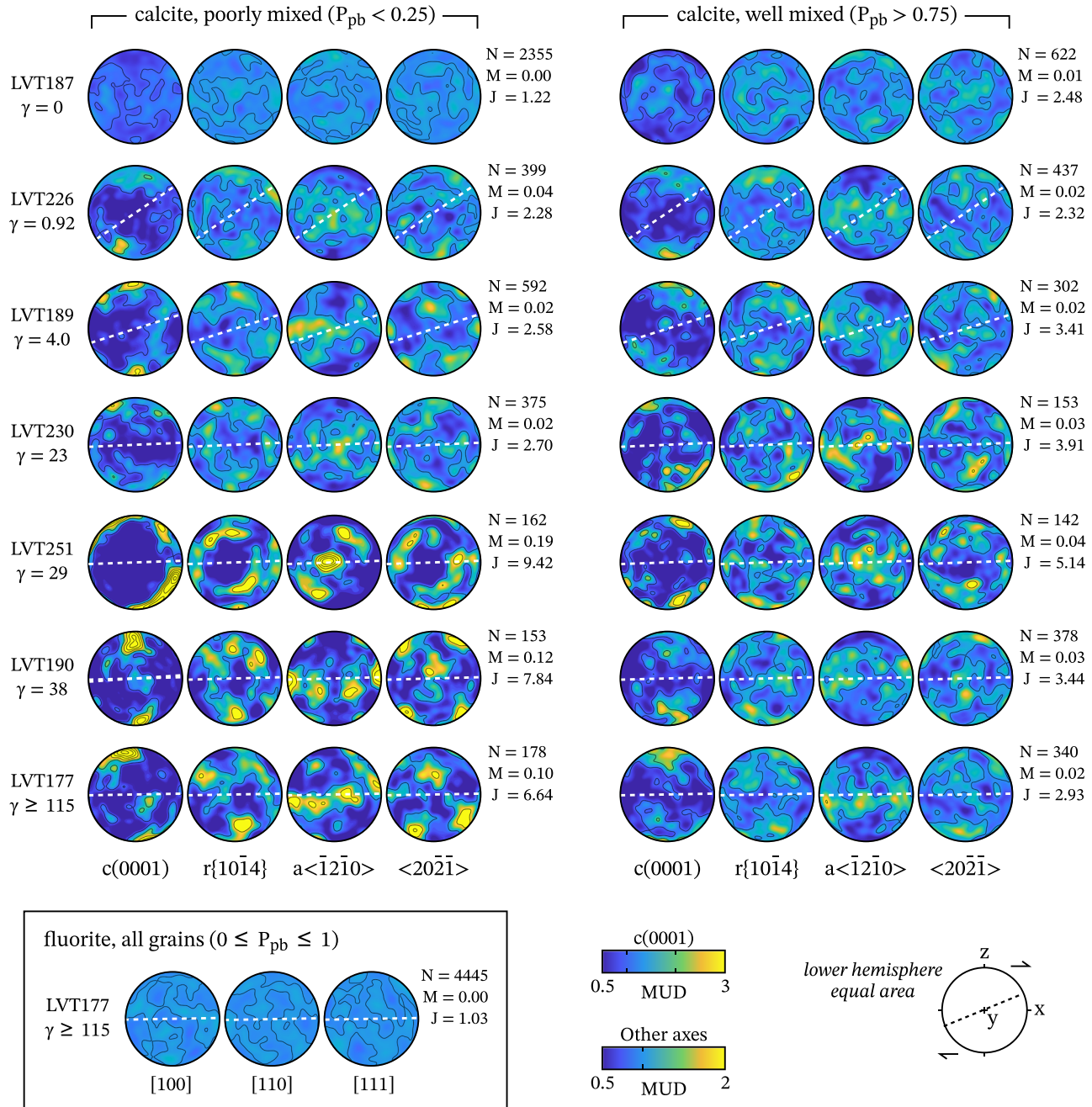


**Figure 5.** Contoured pole figures for calcite in the  $\text{Ca}_{50}\text{-Fl}_{50}$  samples. Strain increases downward. Calcite grains have been divided into poorly mixed (phase boundary fraction,  $P_{pb} < 0.25$ ; left column) and well-mixed ( $P_{pb} > 0.75$ ; right column) populations. Inset: a representative set of pole figures for fluorite grains in the highest strain sample (see Figure S3 for the full set of fluorite pole figures). Pole figures are lower-hemisphere, equal-area projections, constructed using one-point-per-grain (mean grain orientation) data, contoured using a  $7.5^\circ$  cone half-width. The number of grains,  $N$ , is given to the right of each pole figure set, along with fabric strength measures—the M-index (Skemer et al., 2005) and J-index (Bunge, 1982)—calculated from the all-points-per-grain data.

namely, by diffusion creep, which necessarily involves a component of grain boundary sliding (Stevens, 1971) that can weaken CPOs (Bestmann & Prior, 2003; Cross et al., 2017; Zhang et al., 1994). In the calcite-anhydrite experiments, for instance, calcite CPOs in well-mixed regions became progressively weaker with increasing strain, which Cross and Skemer (2017) attributed to an increasing contribution of grain-size-sensitive deformation.

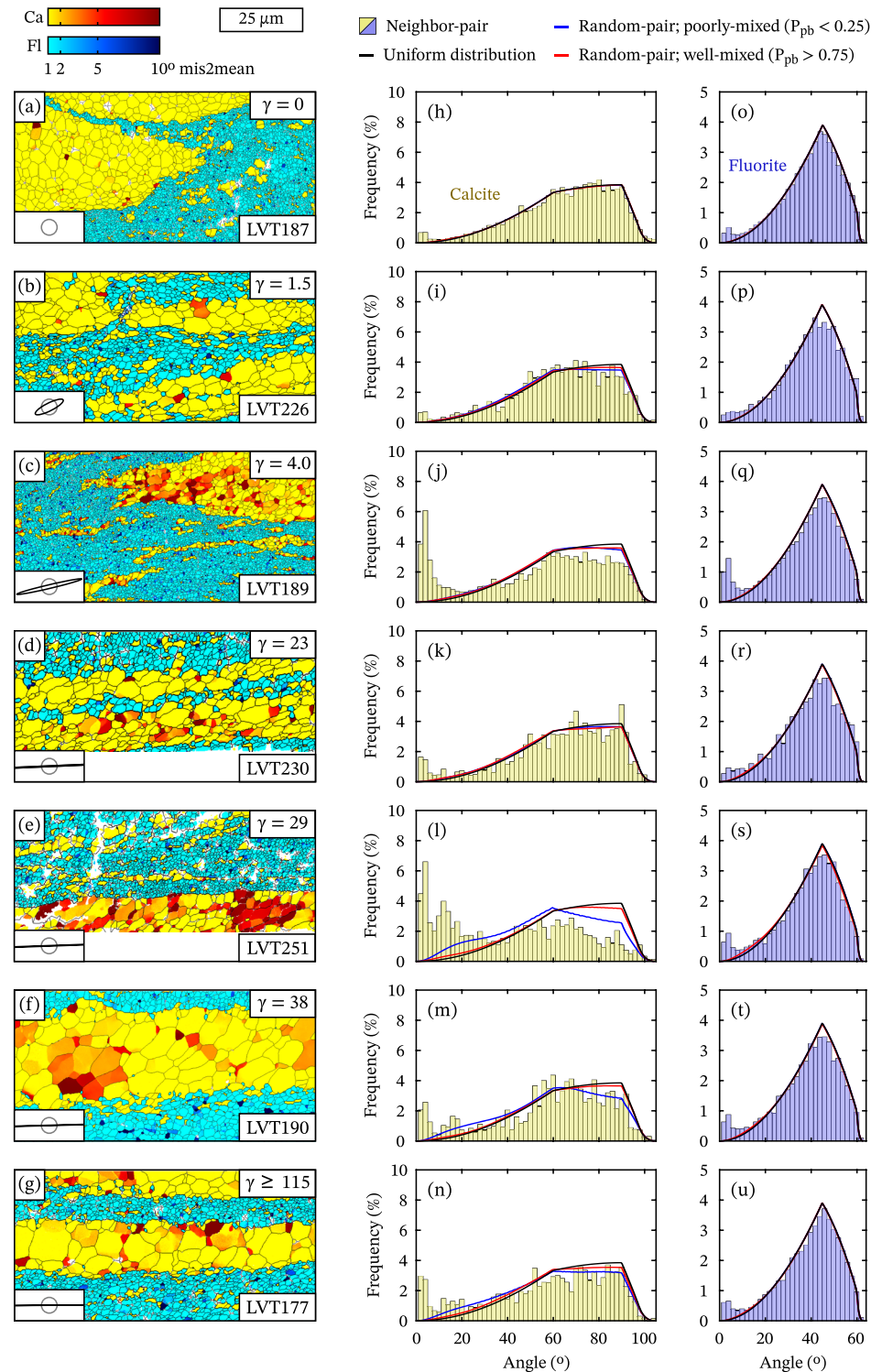


**Figure 6.** Misorientation data for the  $\text{Ca}_{50}\text{-Fl}_{50}$  samples (see Figure S4 for  $\text{Ca}_{20}\text{-Fl}_{80}$  samples). (a–g) Maps of mis2mean (the misorientation angle between each pixel in a grain and that grain's mean orientation) for calcite (hot colors) and fluorite (cool colors). Grain boundaries ( $\geq 10^\circ$  misorientation) and interphase boundaries are shown in black. The finite strain ellipse for each experiment is shown in the lower left of each map. Dextral shear sense (top-to-the-right). Strain increases downward. Corresponding misorientation distribution functions (MDFs) for (h–n) calcite and (o–u) fluorite show the angle distributions of neighbor-pair (correlated) misorientations (histograms), and random-pair (uncorrelated) misorientations in poorly-mixed (blue curve) and well-mixed (red curve) grains, compared to the theoretical uniform misorientation distribution function (black curve).



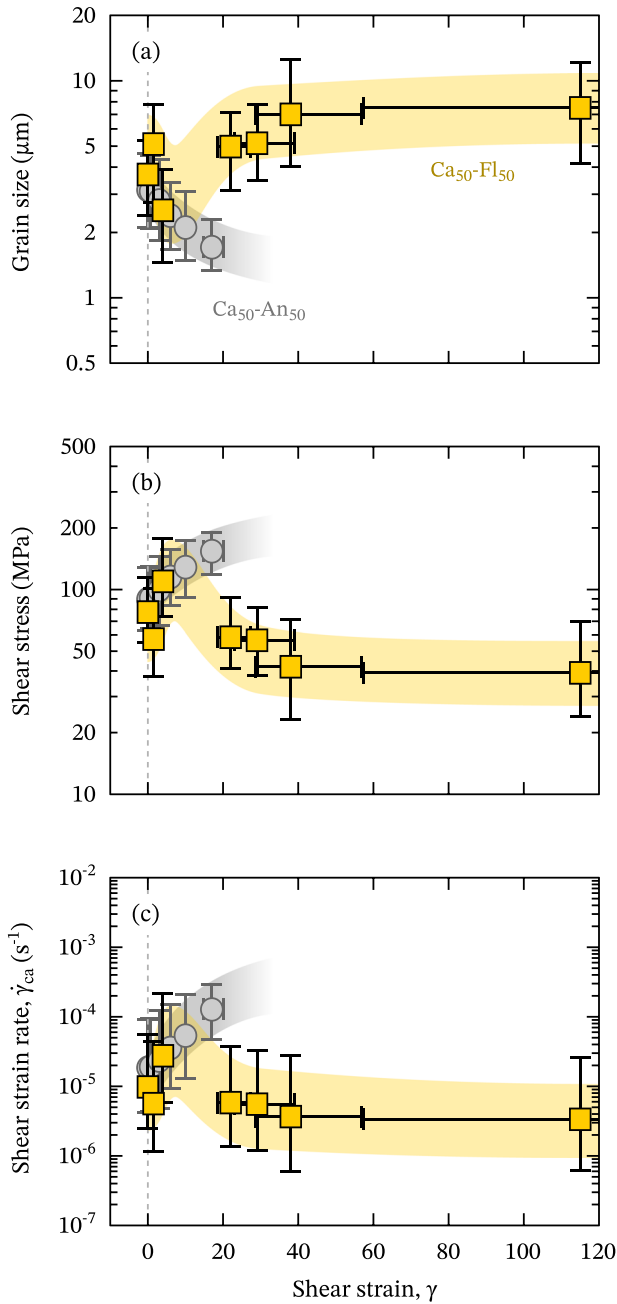


**Figure 7.** The micromechanical evolution of poorly-mixed calcite grains in the calcite-anhydrite (gray circles) and  $\text{Ca}_{50}\text{-Fl}_{50}$  (yellow squares) experiments. Both sets of experiments were conducted under nominally the same conditions (500°C temperature;  $10^{-5}$ – $10^{-4}$   $\text{s}^{-1}$  bulk strain rate). (a) Poorly-mixed calcite grain size in calcite-anhydrite samples (Cross & Skemer, 2017) and calcite-fluorite samples (this study, Figure 4a). Vertical error bars represent the interquartile range in grain size. (b) Shear stresses, calculated using the calcite paleowattmeter (Austin & Evans, 2007, 2009) and converted from axial stresses using a  $\sqrt{3}$  conversion factor. (c) Shear strain rate calculated using the dislocation and diffusion creep flows for calcite (Herwegh et al., 2003; Renner et al., 2002) for the grain sizes and stresses shown in (a) and (b), respectively.

#### 4.2. Micromechanical Evolution of Calcite

In the calcite-anhydrite ( $\text{Ca}_{50}\text{-An}_{50}$ ) samples, poorly-mixed calcite grains underwent monotonic grain size reduction with increasing strain (Figure 7a, gray circles). In the  $\text{Ca}_{50}\text{-Fl}_{50}$  samples, however, poorly mixed calcite grains initially underwent grain size reduction, before coarsening markedly at intermediate to large strains (Figure 7a, yellow squares). Grain coarsening indicates either a decrease in differential stress or a decrease in deformation work rate, following paleopiezometer (e.g., Derby & Ashby, 1987) or paleowattmeter (Austin & Evans, 2007) models, respectively.

Cross and Skemer (2017) found that poorly-mixed calcite grain sizes were best described by the calcite paleowattmeter. We therefore calculate the evolution of differential stress (Figure 7b) and strain rate (Figure 7c) in poorly mixed calcite domains, using the grain sizes discussed above (Figure 4a) in conjunction with the calcite paleowattmeter of Austin and Evans (2007, 2009) and the calcite dislocation and diffusion creep flow laws of Renner et al. (2002) and Herwegh et al. (2003), respectively.

In both the  $\text{Ca}_{50}\text{-An}_{50}$  and  $\text{Ca}_{50}\text{-Fl}_{50}$  samples, poorly-mixed calcite grains underwent modest grain size reduction from a median grain size of  $\sim 4$   $\mu\text{m}$  at  $\gamma = 0$ , to a median grain size of  $\sim 2$   $\mu\text{m}$  at  $\gamma = 4$  (Figure 7a). For a 2  $\mu\text{m}$  grain size and 500°C experimental run temperature, the calcite paleowattmeter predicts a shear stress of  $\sim 100$  MPa (Figure 7b), which in turn gives a shear strain rate of  $\sim 3 \times 10^{-5}$   $\text{s}^{-1}$  using the calcite flow laws (Figure 7c). Beyond  $\gamma = 4$ , the calcite-anhydrite and calcite-fluorite samples followed diverging micromechanical paths. Poorly-mixed calcite grains in the calcite-anhydrite samples continued to recrystallize, reaching steady state deformation at a shear stress of  $\sim 150$  MPa and shear strain rate of  $\sim 2 \times 10^{-4}$   $\text{s}^{-1}$  (Figures 7b and 7c, gray circles). In the calcite-fluorite samples, on the other hand, poorly-mixed calcite grains coarsened to a median size of 8  $\mu\text{m}$  at  $\gamma > 50$ . This grain size corresponds to a shear stress of  $\sim 40$  MPa (Figure 7b, yellow squares) and shear strain rate of  $\sim 3 \times 10^{-6}$   $\text{s}^{-1}$  (Figure 7c, yellow squares). Note, for comparison, that similar conditions are derived for the  $\text{Ca}_{20}\text{-Fl}_{80}$  samples ( $\sim 50$  MPa and  $\sim 2 \times 10^{-6}$   $\text{s}^{-1}$ —see Figure S5); however, the  $\text{Ca}_{20}\text{-Fl}_{80}$  samples underwent continuous, modest grain size reduction with increasing strain, with no evidence for hardening at low to intermediate strains.

#### 4.3. Degree of Strain Partitioning

The shear strain rates calculated for calcite domains ( $\sim 10^{-5}$ – $10^{-6}$   $\text{s}^{-1}$ ; Figures 7c and S5) are significantly lower than the bulk shear strain rates of the calcite-fluorite samples ( $10^{-4}$ – $10^{-5}$   $\text{s}^{-1}$ ; Table 1). To maintain strain compatibility during constant volume deformation, bulk strain rate is given by the volume-weighted sum of strain rates in the individual phases (Bloomfield & Covey-Crump, 1993; Handy, 1994):

$$\dot{\gamma}_{\text{bulk}} = \sum_{i=1}^N \phi_i \dot{\gamma}_i = \phi_{\text{ca}} \dot{\gamma}_{\text{ca}} + \phi_{\text{fl}} \dot{\gamma}_{\text{fl}} \quad (3)$$

where  $\dot{\gamma}$  is shear strain rate and  $\phi$  is the volume fraction of each of the  $N$  phases,  $i$ . To maintain strain compatibility between phases during shear—that is, to prevent void generation at phase domain interfaces—interface slip is required between phases, particularly in the case of a strong

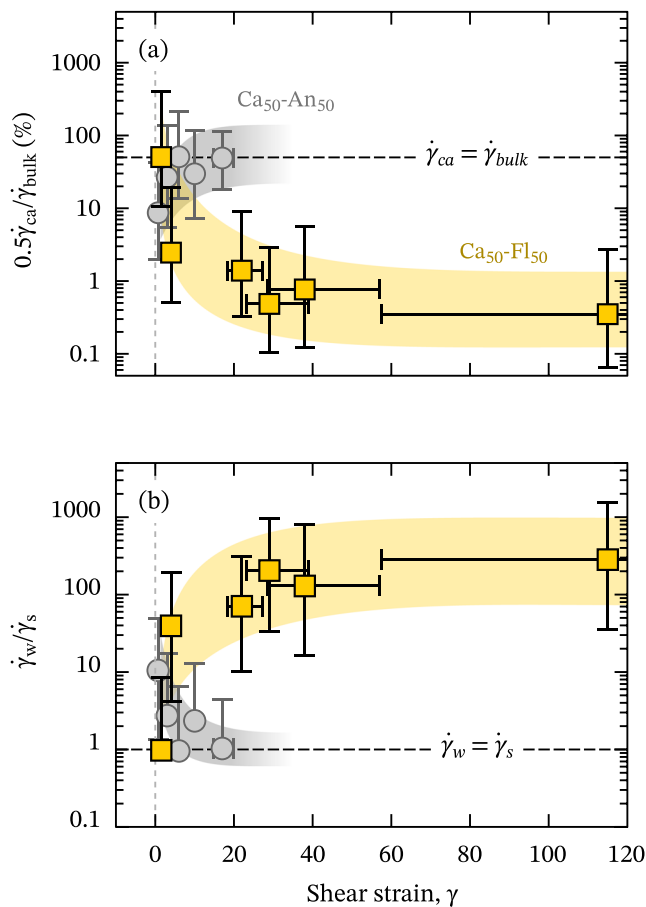


**Figure 8.** Strain partitioning, as a function of shear strain, in the calcite-fluorite (yellow squares) and calcite-anhydrite (gray circles) samples. (a) The percentage of bulk deformation accommodated by poorly mixed calcite regions, weighted by calcite volume fraction. (b) The strain rate ratio between "weak" and "strong" domains. In the nominally isoviscous calcite-anhydrite composites, anhydrite is designated as the "weak" phase, since it deforms faster than calcite at low strains.

phase embedded within a weak framework (Handy, 1994). However, interface slip is not considered a significant strain-producing process in this context, unlike "phase boundary sliding," which may produce strain under specific conditions where deformation is rate-limited by interface reactions or diffusion in pseudo-binary materials (Sundberg & Cooper, 2008; Zhao et al., 2019). Phase boundary sliding is expected to promote a marked increase in phase boundary density (Zhao et al., 2019), which we do not see here (Figure 3). Furthermore, we observe no clear or systematic strain marker offsets across phase boundaries and therefore assume that deformation was primarily accommodated by the intracrystalline creep of calcite and fluorite, per Equation 3.

Here, fluorite shear strain rate,  $\dot{\gamma}_f$ , is the only remaining unknown. Strain markers provide the bulk shear strain rate,  $\dot{\gamma}_{bulk}$ , of each sample (Table 1), calcite grain sizes and flow laws give  $\dot{\gamma}_{ca}$  (Figure 7c), and the phase fractions are set at  $\phi_{ca} = \phi_{fl} = 0.5$  for the  $Ca_{50}-Fl_{50}$  samples. Thus, from Equation 3, we see that calcite deformation accounts for only  $\leq 1\%$  of the bulk strain rate in our highest strain samples (yellow squares, Figure 8a), where  $\dot{\gamma}_{bulk} \approx 4 \times 10^{-4} \text{ s}^{-1}$  (Table 1) and  $\dot{\gamma}_{ca} \approx 3 \times 10^{-6} \text{ s}^{-1}$  (Figure 7c). Likewise, in the  $Ca_{20}-Fl_{80}$  samples, we estimate that calcite accommodated only 1% of the total deformation (Figure S6a). The majority of deformation, we infer, was therefore accommodated within fluorite-rich domains. In fact, Equation 3 reveals that in the  $Ca_{50}-Fl_{50}$  samples, fluorite domains accommodated an increasing percentage of the overall deformation with increasing strain (yellow squares, Figure 8b)—at the onset of deformation ( $\gamma < 1$ ), calcite and fluorite deformed at nominally the same rate, but at large strains ( $\gamma \gg 10$ ), fluorite deformed up to 300 times faster than calcite (Figure 8b). In the  $Ca_{20}-Fl_{80}$  samples, on the other hand, the degree of strain partitioning did not change significantly with strain; fluorite consistently deformed 100–200 times faster than calcite (Figure S6b).

These calculations raise an interesting paradox: calcite domains are elongated and align with the bulk finite strain ellipse in each sample (Figures 1m and 1n), yet calcite apparently deformed much more slowly than fluorite and, likewise, far below the bulk shear strain rate. Indeed, by integrating the calculated calcite strain rates (Figure 7c) over the duration of each experiment, we obtain a maximum finite shear strain of only

$1.84^{+11.5}_{-1.46}$ —that is, no greater than 14—in calcite domains of the high-strain  $Ca_{50}-Fl_{50}$  samples (Figures S7a–S7b). Similarly, we obtain a maximum finite shear strain of  $0.70^{+4.1}_{-0.57}$  for calcite domains in the  $Ca_{20}-Fl_{80}$  samples (Figures S7c–S7d). Further evidence that calcite domains did not deform to large shear strains arises from the thicknesses of calcite layers in the highly deformed  $Ca_{50}-Fl_{50}$  samples. In order for an initially spherical domain to preserve a thickness of  $>50 \mu\text{m}$  at  $\gamma = 38$  (Figure 1m), it would need to have an initial diameter of  $\sim 2,000 \mu\text{m}$  at  $\gamma = 0$ , according to Ramsay's (1980) equations for the change in shape of a sheared circular marker (Figure S8a). Considering that our specimens were initially only  $500 \mu\text{m}$  thick, this is not possible. If, however, calcite domains were sheared to  $\gamma = 10$  or less—and rotated into the shear plane as semi-rigid layers or ellipses thereafter—their starting diameters would need to be no greater than the thickness of our samples (Figure S8b).

Although fluorite deformed 100–300 times faster than calcite in both the  $Ca_{20}-Fl_{80}$  and  $Ca_{50}-Fl_{50}$  experiments, the degree of strain partitioning increased (with increasing strain) in the  $Ca_{50}-Fl_{50}$  samples (Figure 8b). We propose that the degree of strain partitioning depended on the degree of weak phase (fluorite) interconnectivity. In the  $Ca_{20}-Fl_{80}$  samples, fluorite occupied a large volume of the sample so was able to form a through-going weak network even at small strains. In the  $Ca_{50}-Fl_{50}$  experiments, on the other hand, strain partitioning became more pronounced as compositional, shear plane-parallel layering formed at low

to intermediate strains ( $\gamma \leq 10$ ). Given that calcite and fluorite initially deformed at similar rates in the Ca<sub>50</sub>-Fl<sub>50</sub> samples (Figure 8b), we infer that the Ca<sub>50</sub>-Fl<sub>50</sub> samples evolved from near-isostrain (i.e., phases deform at the same rate) to near-isostress (i.e., phases deform at the same stress) conditions with increasing strain, as compositional layering developed. Indeed, shear plane-parallel layers (e.g., Figures 1m and 1n) are optimally oriented for isostress deformation in simple shear (Gerbi et al., 2016; Hutchinson, 1976; Jessell et al., 2009), where the weakest interconnected phase deforms fastest. Curiously, the strongly layered Ca<sub>50</sub>-Fl<sub>50</sub> samples were able to deform to large bulk shear strains without significant necking, buckling, or boudinage, despite the substantial inferred degree of strain partitioning (cf., Bons & Cox, 1994; Dabrowski & Grasemann, 2014).

#### 4.4. Calcite-Fluorite Viscosity Contrast

Having placed constraints on the strain rates of calcite- and fluorite-rich domains, we can now estimate the viscosity contrast between the phases. Viscosity contrast is defined as

$$\frac{\eta_s}{\eta_w} = \frac{\tau_s \dot{\gamma}_w}{\dot{\gamma}_s \tau_w} \quad (4)$$

where the subscripts *s* and *w* indicate the strong and weak phase, respectively. In order to estimate viscosity contrast, we must therefore make assumptions about stress and strain rate partitioning between the two phases. Limiting values are given by assuming isostress (Sachs bound) or isostrain (Taylor bound) conditions. As mentioned above, we infer that the Ca<sub>50</sub>-Fl<sub>50</sub> samples deformed under near-isostress conditions at large strains, producing significant strain partitioning. Thus, by assuming  $\tau_s = \tau_w$ , we obtain an upper limit on viscosity contrast of  $\eta_{ca}/\eta_{fl} = 300$  for a strain rate contrast of  $\dot{\gamma}_{fl}/\dot{\gamma}_{ca} = 300$  in the Ca<sub>50</sub>-Fl<sub>50</sub> samples (Figure 8b).

As a second estimate of viscosity contrast, we adopt Handy's (1990, 1994) model for strain partitioning in a two-phase composite. Handy's (1994) approach, which is rooted in minimizing viscous strain energy, provides flow laws for two-phase composites in which load is supported by either the strong or weak phase: the so-called load-bearing framework (LBF) and interconnected weak layer (IWL) cases, respectively. In the LBF state, both phases are assumed to deform at the same rate, whereas in the IWL state, strain localizes into the weak phase. LBF structures deform under isostrain conditions, whereas IWL structures lie close to the isostress bound (Handy, 1994). For IWL structures, the strain rate contrast between weak and strong phases,  $\dot{\gamma}_w/\dot{\gamma}_s$ , is given as follows:

$$\frac{\dot{\gamma}_w}{\dot{\gamma}_s} = \frac{1 - \phi_w}{\phi_w^x - \phi_w} \quad (5)$$

where  $\phi_w$  is the weak phase volume fraction and *x* is a strain partitioning parameter defined as

$$x = 1 - \frac{1}{\eta_s/\eta_w} \quad (6)$$

The strain partitioning parameter is defined such that  $x \rightarrow 0$  when  $\eta_s/\eta_w \rightarrow 1$  (i.e., no strain partitioning for isoviscous composites), and  $x \rightarrow 1$  when  $\eta_s/\eta_w \rightarrow \infty$  (i.e., complete strain partitioning for infinitely nonisoviscous composites). Note that the functional form of *x* between these limits is not constrained nor does it explicitly account for phase morphology (e.g., phase domain aspect ratio and orientation), strain, loading geometry, and phase connectivity. However, our strongly layered high-strain samples closely resemble the ideal IWL structure modeled by Handy (1994), which we therefore assume provides a reasonable estimate of the calcite-fluorite viscosity contrast. By rearranging Equations 5 and 6,  $\eta_s/\eta_w$  can be expressed as a function of  $\phi_w$  and  $\dot{\gamma}_w/\dot{\gamma}_s$ :

$$\frac{\eta_s}{\eta_w} = \left[ 1 - \ln \left( \frac{1 - \phi_w}{\dot{\gamma}_w/\dot{\gamma}_s + \phi_w} \right) (\ln \phi_w)^{-1} \right]^{-1} \quad (7)$$



Taking  $\phi_w = 0.5$  and  $\dot{\gamma}_f/\dot{\gamma}_{ca} \approx 300$  (Figure 8b), we obtain a second estimate on the calcite-fluorite viscosity contrast of  $\eta_{ca}/\eta_f \approx 200$  under our experimental conditions.

#### 4.5. Influence of Viscosity Contrast and Strain Partitioning on Phase Mixing Timescales

In the calcite-anhydrite experiments performed by Cross and Skemer (2017), phase mixing progressed by the geometric shearing of polycrystalline phase domains to form compositional layering (Figures 1a–1e). With increasing shear strain, compositional layers became increasingly stretched and attenuated (Figure 1f), leading ultimately to their disaggregation and the formation of a fine-grained, well-mixed ultramylonite (Figure 1g). Cross and Skemer (2017) found that, to first order, the critical strain required for geometric mixing,  $\gamma_c$ , was directly related to the ratio between the initial thickness of phase domains,  $w_i$  (measured perpendicular to the shear plane) and the critical thickness at which compositional layers became disaggregated,  $w_c$  (nominally equivalent to the pinned, recrystallized grain size of the two-phase mixture):

$$\gamma_c \approx \frac{w_i}{w_c} \quad (8)$$

In the calcite-fluorite samples examined here, however, extensive phase mixing is not observed, even at equally large shear strains ( $\gamma \geq 50$ ) and even though the ratio  $w_i/w_c$  is very similar to that of the calcite-anhydrite samples. We suggest that in the nonisoviscous calcite-fluorite samples, geometric phase mixing was inhibited by the localization of deformation into the weaker phase, fluorite, slowing the rate of calcite layer attenuation and disaggregation. Microstructural analyses, outlined above, suggest that calcite layers did not deform to shear strains greater than  $\sim 14$  (Figure S7), and accommodated only  $\leq 1\%$  of the deformation at large strains (Figure 8a). These observations are consistent with numerical models (Gardner et al., 2017; Jessell et al., 2009), field observations (Stenvall et al., 2019), and experiments (Bons & Urai, 1994; Holyoke & Tullis, 2006) showing strain localization into interconnected weak layers. In fact, some numerical models of two-phase deformation predict initial hardening at low strains ( $\gamma \approx 1$ )—as second phase inclusions become elongated and oriented subperpendicular to the instantaneous stretching direction—followed by softening to large strains as interconnected weak layers develop (Dabrowski et al., 2012; Takeda & Grier, 2006). Remarkably similar behavior is observed here, with peak stresses reached at low shear strains in the Ca<sub>50</sub>-Fl<sub>50</sub> samples (Figures 7b and 7c), before the onset of softening and strain partitioning coinciding with compositional layer formation. In the Ca<sub>20</sub>-Fl<sub>80</sub> samples on the other hand, no conspicuous hardening stage is observed (Figure S5), presumably because fluorite—occupying a larger fraction (i.e., 80%) of the sample volume—formed a weak interconnected network even at very small strains.

To account for the effects of viscosity contrast on geometric phase mixing timescales, we propose the following modification to Equation 8:

$$\gamma_c \approx \frac{w_i \dot{\gamma}_w}{w_c \dot{\gamma}_s} \quad (9)$$

such that geometric phase mixing is more protracted when strain partitioning—represented by the strain rate contrast between weak and strong phase domains,  $\dot{\gamma}_w/\dot{\gamma}_s$ —reduces the rate at which strong domains deform, attenuate, and disaggregate. It is important to note that in isoviscous composites, or under iso-strain conditions,  $\dot{\gamma}_w/\dot{\gamma}_s = 1$ , and Equation 8 converges with Equation 9. Conversely, as  $\dot{\gamma}_w/\dot{\gamma}_s \rightarrow \infty$ , geometric phase mixing becomes impossible ( $\gamma_c \rightarrow \infty$ ). Equation 9 does not account for grain-scale “tooth” mixing (Bercovici & Skemer, 2017), which, as highlighted by our Ca<sub>20</sub>-Fl<sub>80</sub> experiments (Figures 10–11), does not produce extensive phase mixing; that is, mixing extending more than one or two grain length scales from a given phase domain boundary (Figure 2).

Equation 9 highlights the protracted nature and relative inefficiency of mechanical (geometric) phase mixing. As shown in Cross and Skemer (2017),  $w_i/w_c$  values are typically on the order of 10–100 for lithospheric shear zones. Thus, in order to achieve extensive mechanical mixing on a reasonable geologic timescale, deformation must occur under conditions that minimize strain partitioning ( $\dot{\gamma}_w/\dot{\gamma}_s < 10$ ). Some studies suggest, for instance, that strain partitioning is more pronounced under constant stress boundary conditions (Fressengeas & Molinari, 1987; Hansen, Zimmerman, Dillman, et al., 2012; Paterson, 2007). Under constant strain rate boundary conditions (like those imposed here), on the other hand, strain partitioning may not

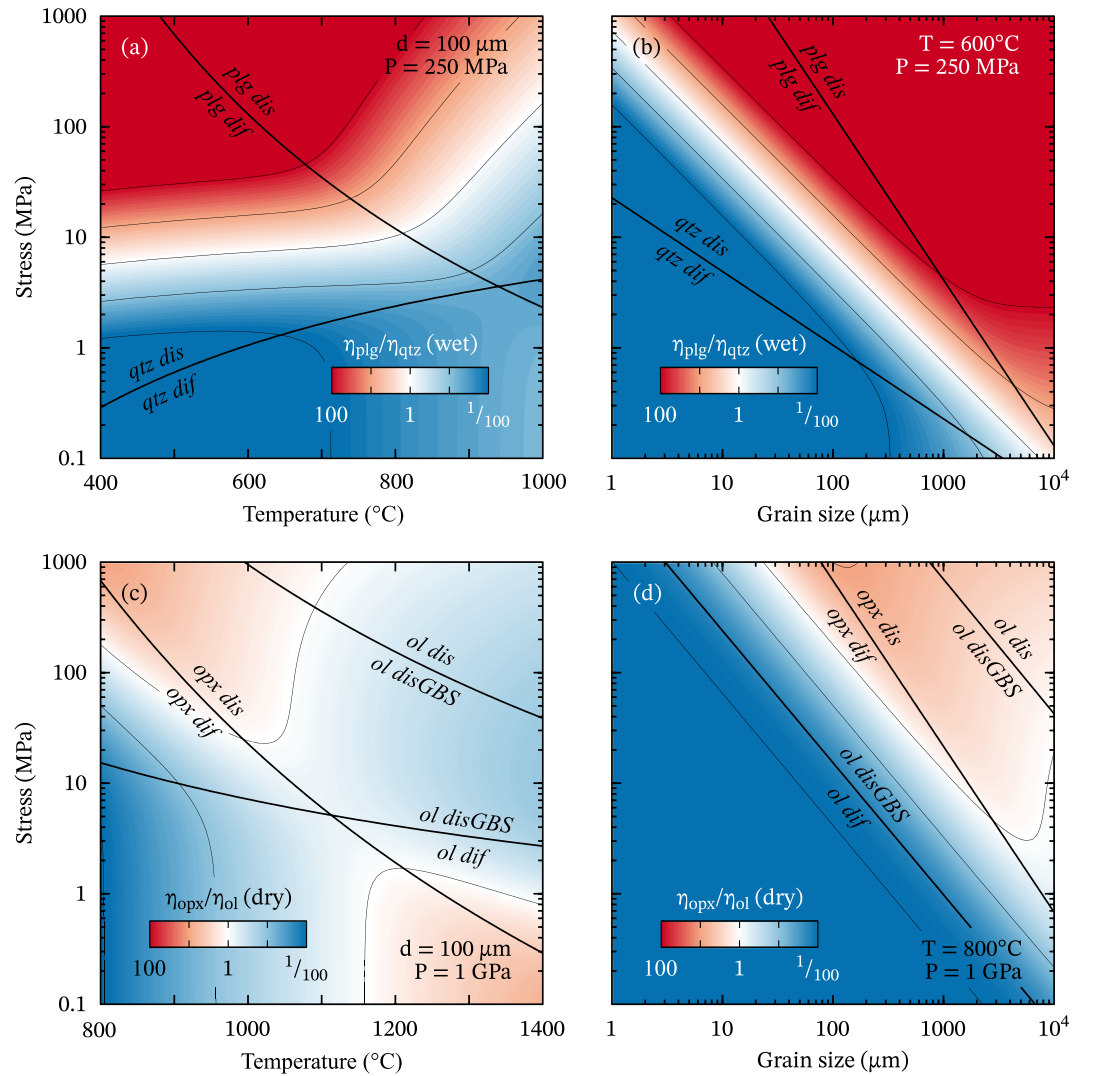


**Figure 9.** Viscosity contrast maps for (a–b) wet quartz-plagioclase and (c–d) dry olivine-enstatite lithologies, as a function of (a, c) stress and temperature and (b, d) stress and grain size. Red regions correspond to conditions where plagioclase and orthopyroxene are stronger than quartz and olivine, respectively. Dark contours show the deformation mechanism field boundaries of the phases (dis = dislocation creep, disGBS = dislocation-accommodated grain boundary sliding, dif = diffusion creep). Details on the viscosity contrast calculations and flow laws are given in Text S1 and Table S1. Small viscosity contrasts correspond to regions of parameter space where mechanical phase mixing is most efficient and where ultramylonites should form most readily. Large viscosity contrasts correspond to regions of parameter space where mechanical phase mixing is relatively inefficient and where phase mixing and ultramylonite formation will be inhibited.

occur unless a threshold viscosity contrast is reached (Hansen, Zimmerman, Dillman, et al., 2012), in which case  $\dot{\gamma}_w/\dot{\gamma}_s$  and  $\gamma_c$  will be minimized. Furthermore, given that chemical phase mixing mechanisms are capable of producing well-mixed ultramylonites over considerably shorter timescales (e.g., Mansard et al., 2020), Equation 9 should be considered as providing an absolute upper bound on phase mixing timescales.

#### 4.6. What Conditions Promote Mechanical Phase Mixing in Nature?

We propose that mature, ultramylonite-bearing shear zones and plate boundaries form most efficiently when viscosity contrasts are minimized (Equation 9). To briefly examine the conditions favoring mechanical phase mixing in natural systems, we calculate viscosity contrast as a function of stress, grain size, and temperature for quartz-feldspar (i.e., crustal) and olivine-pyroxene (i.e., mantle) lithologies under both wet and

dry conditions (Figures 9 and S9). Viscosities are calculated using laboratory flow laws for quartz (Rutter & Brodie, 2004; Tople et al., 2019), plagioclase (Rybacki & Dresen, 2004), Mg-rich olivine (Hansen et al., 2011; Hirth & Kohlstedt, 2003; Ohuchi et al., 2015), and enstatite (Bystricky et al., 2016; Ross & Nielsen, 1978; Zhang et al., 2017). Water fugacities are calculated as a function of temperature and pressure following Shinevar et al. (2015). Details on the viscosity contrast calculations and flow law parameters are provided in Text S1 and Table S1. For the sake of simplicity, we assume isostress conditions, which, as discussed above, is a reasonable approximation in strongly foliated, high-strain rocks.

Our calculations show that viscosity contrast varies by many orders of magnitude under natural conditions. In wet quartzofeldspathic rocks, laboratory flow laws suggest that feldspar is two or more orders of magnitude stronger than quartz under high stress, low temperature conditions (Figure 9a), particularly at grain sizes  $>100\text{ }\mu\text{m}$  under typical crustal stresses ( $>10\text{ MPa}$ ) (Figure 9b). However, quartz appears significantly stronger than feldspar when both phases are deforming by diffusion creep. “Ideal” conditions for mechanical mixing are found under wet middle to lower crust conditions— $400\text{--}800^\circ\text{C}$ ,  $10\text{--}100\text{ MPa}$  stress,  $10\text{--}100\text{ }\mu\text{m}$  grain size—where both phases have similar viscosities ( $\eta_{\text{plg}}/\eta_{\text{qtz}} < 10$ ). It is worth noting that under dry conditions, feldspar is  $100\text{--}1,000$  times stronger than quartz for all typical stresses, grain sizes, and temperatures  $<800^\circ\text{C}$  (Figures S9a and S9b).

Viscosity contrasts are generally smaller in dry olivine-orthopyroxene aggregates over mantle lithosphere conditions (Figures 9c and 9d). In particular, viscosity contrasts are modest ( $\eta_{\text{opx}}/\eta_{\text{ol}} \leq 10$ ) under low temperature, high stress conditions ( $800\text{--}1000^\circ\text{C}$ ,  $10\text{--}500\text{ MPa}$ ), and high-temperature, low stress conditions ( $1200\text{--}1400^\circ\text{C}$ ,  $0.1\text{--}10\text{ MPa}$ ), that is, at typical conditions for upper mantle shear zones and the lithosphere-asthenosphere boundary, respectively. Under wet conditions, however, olivine is predicted to be significantly stronger than enstatite ( $\eta_{\text{opx}}/\eta_{\text{ol}} < 0.01$ ) except at high temperatures ( $>1200^\circ\text{C}$ ) and stresses ( $>100\text{ MPa}$ ) (Figures S9c and S9d). While wet conditions therefore appear unsuitable for mechanical mixing, such conditions may significantly enhance chemical mixing mechanisms by providing free fluids and fast diffusive networks for chemical exchange and mass transfer.

## 5. Summary and Closing Remarks

To examine the influence of viscosity contrast on phase mixing during high-temperature creep, we deformed polycrystalline, poorly mixed composites of calcite and fluorite to large shear strains in torsion. As in comparable experiments on isoviscous calcite-anhydrite samples, the nonisoviscous calcite-fluorite composites developed a well-defined compositional layering at low to intermediate strains ( $\gamma \leq 10$ ) due to the collective shearing of phase domains. However, whereas compositional layers became increasingly stretched and attenuated in the calcite-anhydrite samples—leading ultimately to their disaggregation and the formation of a well-mixed ultramylonite—compositional layers are retained to large shear strains ( $\gamma > 50$ ) in the calcite-fluorite samples. Local, grain-scale phase mixing by grain switching across phase boundaries is also observed but did not produce extensive phase mixing. Strain rates and stresses calculated using paleowattmetry and calcite flow laws indicate that deformation became increasingly partitioned into weak, interconnected fluorite layers with increasing bulk shear strain, deforming under near-isostress conditions. At large strains, calcite deformation accounted for  $\leq 1\%$  of the overall bulk deformation, implying a viscosity contrast of  $200\text{--}300$ . Strain partitioning slowed the stretching and attenuation of calcite layers, thereby inhibiting geometric mixing. Our experiments suggest that mechanical phase mixing can be extremely protracted and is likely superseded by chemical phase mixing under most conditions, except where metamorphic reactions, chemical exchange, and diffusive mass transfer are sluggish, for instance in the cold, dry lithosphere. Nevertheless, “ideal” conditions for mechanical (geometric) phase mixing may be found in the wet middle to lower continental crust, and the dry mantle lithosphere, where quartz-plagioclase and olivine-pyroxene viscosity contrasts are minimized, respectively.

## Data Availability Statement

The BSE images and EBSD data used in this study are available on the Woods Hole Open Access Server (WHOAS; <https://doi.org/10.26025/1912/25940>).



## Acknowledgments

This work was funded through a National Science Foundation grant (EAR-1352306) awarded to P. S., with additional support for A. J. C. provided by the McDonnell Center for the Space Sciences (Washington University in St. Louis), the J. Lamar Worzel Assistant Scientist Fund (WHOI), and the Penzance Endowed Fund in Support of Assistant Scientists (WHOI). Partial support for electron microscopy was provided by the Institute of Materials Science and Engineering (Washington University in St. Louis). We thank J. Précigout and one anonymous reviewer for constructive reviews.

## References

- Audet, P., & Bürgmann, R. (2011). Dominant role of tectonic inheritance in supercontinent cycles. *Nature Geoscience*, 4, 184–187. <https://doi.org/10.1038/ngeo1080>
- Austin, N. J., & Evans, B. (2007). Paleowattmeters: A scaling relation for dynamically recrystallized grain size. *Geology*, 35, 343. <https://doi.org/10.1130/G23244A.1>
- Austin, N. J., & Evans, B. (2009). The kinetics of microstructural evolution during deformation of calcite. *Journal of Geophysical Research*, 114, B09402. <https://doi.org/10.1029/2008JB006138>
- Bachmann, F., Hielscher, R., & Schaefer, H. (2010). Texture analysis with MTEX—Free and open source software toolbox. *Solid State Phenomena*, 160, 63–68. <https://doi.org/10.4028/www.scientific.net/SSP.160.63>
- Barnhoorn, A., Bystricky, M., Burlini, L., & Kunze, K. (2004). The role of recrystallisation on the deformation behaviour of calcite rocks: Large strain torsion experiments on Carrara marble. *Journal of Structural Geology*, 26, 885–903. <https://doi.org/10.1016/j.jsg.2003.11.024>
- Bercovici, D., & Ricard, Y. (2014). Plate tectonics, damage and inheritance. *Nature*, 508, 513–516. <https://doi.org/10.1038/nature13072>
- Bercovici, D., & Ricard, Y. (2016). Grain-damage hysteresis and plate tectonic states. *Physics of the Earth and Planetary Interiors*, 253, 31–47. <https://doi.org/10.1016/j.pepi.2016.01.005>
- Bercovici, D., & Skemer, P. (2017). Grain damage, phase mixing and plate-boundary formation. *Journal of Geodynamics*, 108, 40–55. <https://doi.org/10.1016/j.jog.2017.05.002>
- Bestmann, M., & Prior, D. J. (2003). Intragranular dynamic recrystallization in naturally deformed calcite marble: Diffusion accommodated grain boundary sliding as a result of subgrain rotation recrystallization. *Journal of Structural Geology*, 25, 1597–1613. [https://doi.org/10.1016/S0191-8141\(03\)00006-3](https://doi.org/10.1016/S0191-8141(03)00006-3)
- Bloomfield, J. P., & Covey-Crump, S. J. (1993). Correlating mechanical data with microstructural observations in deformation experiments on synthetic two-phase aggregates. *Journal of Structural Geology*, 15, 1007–1019. [https://doi.org/10.1016/0191-8141\(93\)90173-8](https://doi.org/10.1016/0191-8141(93)90173-8)
- Bons, P. D., & Cox, S. J. D. (1994). Analogue experiments and numerical modelling on the relation between microgeometry and flow properties of polyphase materials. *Materials Science and Engineering A*, 175, 237–245. [https://doi.org/10.1016/0921-5093\(94\)91063-4](https://doi.org/10.1016/0921-5093(94)91063-4)
- Bons, P. D., & Urai, J. L. (1994). Experimental deformation of two-phase rock analogues. *Materials Science and Engineering A*, 175(1–2), 221–229. [https://doi.org/10.1016/0921-5093\(94\)91061-8](https://doi.org/10.1016/0921-5093(94)91061-8)
- Boullier, A. M., & Gueguen, Y. (1975). SP-Mylonites: Origin of some mylonites by superplastic flow. *Contributions to Mineralogy and Petrology*, 50, 93–104. <https://doi.org/10.1007/BF00373329>
- Brun, J. P., & Cobbold, P. R. (1980). Strain heating and thermal softening in continental shear zones: A review. *Journal of Structural Geology*, 2, 149–158. [https://doi.org/10.1016/0191-8141\(80\)90045-0](https://doi.org/10.1016/0191-8141(80)90045-0)
- Bunge, H. (1982). *Texture analysis in materials science: Mathematical models*. London: Butterworths.
- Bystricky, M., Lawlis, J., Mackwell, S., Heidelbach, F., & Raterron, P. (2016). High-temperature deformation of enstatite aggregates. *Journal of Geophysical Research: Solid Earth*, 121, 6384–6400. <https://doi.org/10.1002/2016JB013011>
- Cooper, R. F., & Kohlstedt, D. L. (1986). Rheology and structure of olivine-basalt partial melts. *Journal of Geophysical Research*, 91, 9315. <https://doi.org/10.1029/JB091iB09p09315>
- Cross, A. J., Hirth, G., & Prior, D. J. (2017). Effects of secondary phases on crystallographic preferred orientations in mylonites. *Geology*, 45. <https://doi.org/10.1130/G38936.1>
- Cross, A. J., Kidder, S., & Prior, D. J. (2015). Using microstructures and TitanQ thermobarometry of quartz sheared around garnet porphyroclasts to evaluate microstructural evolution and constrain an Alpine Fault zone geotherm. *Journal of Structural Geology*, 75, 17–31. <https://doi.org/10.1016/j.jsg.2015.02.012>
- Cross, A. J., & Skemer, P. (2017). Ultramylonite generation via phase mixing in high strain experiments. *Journal of Geophysical Research: Solid Earth*, 122, 1744–1759. <https://doi.org/10.1002/2016JB013801>
- Cross, A. J., & Skemer, P. (2019). Rates of dynamic recrystallization in geologic materials. *Journal of Geophysical Research: Solid Earth*, 124, 1324–1342. <https://doi.org/10.1029/2018JB016201>
- Czertowicz, T. A., Toy, V. G., & Scott, J. M. (2016). Recrystallisation, phase mixing and strain localisation in peridotite during rapid extrusion of sub-arc mantle lithosphere. *Journal of Structural Geology*, 88, 1–19. <https://doi.org/10.1016/J.JSG.2016.04.011>
- Dabrowski, M., & Grasemann, B. (2014). Domino boudinage under layer-parallel simple shear. *Journal of Structural Geology*, 68, 58–65. <https://doi.org/10.1016/j.jsg.2014.09.006>
- Dabrowski, M., Schmid, D. W., & Podladchikov, Y. Y. (2012). A two-phase composite in simple shear: Effective mechanical anisotropy development and localization potential. *Journal of Geophysical Research*, 117, B08406. <https://doi.org/10.1029/2012JB009183>
- Derby, B., & Ashby, M. F. (1987). On dynamic recrystallisation. *Scripta Metallurgica*, 21, 879–884. [https://doi.org/10.1016/0036-9748\(87\)90341-3](https://doi.org/10.1016/0036-9748(87)90341-3)
- Dijkstra, A. H., Drury, M. R., Vissers, R. L. M., & Newman, J. (2002). On the role of melt-rock reaction in mantle shear zone formation in the Othris Peridotite Massif (Greece). *Journal of Structural Geology*, 24, 1431–1450. [https://doi.org/10.1016/S0191-8141\(01\)00142-0](https://doi.org/10.1016/S0191-8141(01)00142-0)
- Dixon, J., & Williams, G. (1983). Reaction softening in mylonites from the Arnaboll thrust, Sutherland. *Scottish Journal of Geology*, 19, 157–168. <https://doi.org/10.1144/sjg19020157>
- Drury, M. R., Vissers, R. L. M., Van der Wal, D., & Hoogerduijn Strating, E. H. (1991). Shear localisation in upper mantle peridotites. *Pure and Applied Geophysics*, 137(4), 439–460. <https://doi.org/10.1007/BF00879044>
- Etheridge, M. A., & Wilkie, J. C. (1979). Grain size reduction, grain boundary sliding and the flow strength of mylonites. *Tectonophysics*, 58, 159–178. [https://doi.org/10.1016/0040-1951\(79\)90327-5](https://doi.org/10.1016/0040-1951(79)90327-5)
- Evans, B., Renner, J., & Hirth, G. (2001). A few remarks on the kinetics of static grain growth in rocks. *International Journal of Earth Sciences*, 90, 88–103. <https://doi.org/10.1007/s005310000150>
- Farla, R., Karato, S., & Cai, Z. (2013). Role of orthopyroxene in rheological weakening of the lithosphere via dynamic recrystallization. *Proceedings of the National Academy of Sciences of the United States of America*, 110, 16,355–16,360. <https://doi.org/10.1073/pnas.1218335110>
- Foley, B. J. (2018). On the dynamics of coupled grain size evolution and shear heating in lithospheric shear zones. *Physics of the Earth and Planetary Interiors*, 283, 7–25. <https://doi.org/10.1016/J.PEPI.2018.07.008>
- Fressengeas, C., & Molinari, A. (1987). Instability and localization of plastic flow in shear at high strain rates. *Journal of the Mechanics and Physics of Solids*, 35, 185–211. [https://doi.org/10.1016/0022-5096\(87\)90035-4](https://doi.org/10.1016/0022-5096(87)90035-4)
- Gardner, R., Piazzolo, S., Evans, L., & Daczko, N. (2017). Patterns of strain localization in heterogeneous, polycrystalline rocks—A numerical perspective. *Earth and Planetary Science Letters*, 463, 253–265. <https://doi.org/10.1016/j.epsl.2017.01.039>

- Gerbi, C., Johnson, S. E., Shulman, D., & Klepeis, K. (2016). Influence of microscale weak zones on bulk strength. *Geochemistry, Geophysics, Geosystems*, 17, 4064–4077. <https://doi.org/10.1002/2016GC006551>
- Gilgannon, J., Fusses, F., Menegon, L., Regenauer-Lieb, K., & Buckman, J. (2017). Hierarchical creep cavity formation in an ultramylonite and implications for phase mixing. *Solid Earth*, 8, 1193–1209. <https://doi.org/10.5194/se-8-1193-2017>
- Gilgannon, J., Poulet, T., Berger, A., Barnhoorn, A., & Herwegh, M. (2020). Dynamic recrystallization can produce porosity in shear zones. *Geophysical Research Letters*, 47, e2019GL086172. <https://doi.org/10.1029/2019GL086172>
- Griggs, D. (1967). Hydrolytic weakening of quartz and other silicates\*. *Geophysical Journal International*, 14, 19–31. <https://doi.org/10.1111/j.1365-246X.1967.tb06218.x>
- Gueydan, F., Précigout, J., & Montési, L. G. J. (2014). Strain weakening enables continental plate tectonics. *Tectonophysics*, 631, 189–196. <https://doi.org/10.1016/j.tecto.2014.02.005>
- Handy, M. R. (1990). The solid-state flow of polymineralic rocks. *Journal of Geophysical Research*, 95, 8647. <https://doi.org/10.1029/JB095iB06p08647>
- Handy, M. R. (1994). Flow laws for rocks containing two non-linear viscous phases: A phenomenological approach. *Journal of Structural Geology*, 16, 287–301. [https://doi.org/10.1016/0191-8141\(94\)90035-3](https://doi.org/10.1016/0191-8141(94)90035-3)
- Hansen, L. N., Zimmerman, M. E., Dillman, A. M., & Kohlstedt, D. L. (2012). Strain localization in olivine aggregates at high temperature: A laboratory comparison of constant-strain-rate and constant-stress boundary conditions. *Earth and Planetary Science Letters*, 333–334, 134–145. <https://doi.org/10.1016/j.epsl.2012.04.016>
- Hansen, L. N., Zimmerman, M. E., & Kohlstedt, D. L. (2011). Grain boundary sliding in San Carlos olivine: Flow law parameters and crystallographic-preferred orientation. *Journal of Geophysical Research*, 116, B08201. <https://doi.org/10.1029/2011JB008220>
- Hansen, L. N., Zimmerman, M. E., & Kohlstedt, D. L. (2012). Laboratory measurements of the viscous anisotropy of olivine aggregates. *Nature*, 492(7429), 415–418. <https://doi.org/10.1038/nature11671>
- Herwegh, M., Xiao, X., & Evans, B. (2003). The effect of dissolved magnesium on diffusion creep in calcite. *Earth and Planetary Science Letters*, 212, 457–470. [https://doi.org/10.1016/S0012-821X\(03\)00284-X](https://doi.org/10.1016/S0012-821X(03)00284-X)
- Hiraga, T., Chihiro, T., Ohashi, N., & Sano, S. (2010). Grain growth systematics for forsterite ± enstatite aggregates: Effect of lithology on grain size in the upper mantle. *Earth and Planetary Science Letters*, 291, 10–20. <https://doi.org/10.1016/j.epsl.2009.12.026>
- Hirth, G., & Kohlstedt, D. L. (2003). Rheology of the upper mantle and mantle wedge: A view from the experimentalists. In *Inside the subduction dactory*, *Geophysical Monograph* 138 (pp. 83–105). Washington, DC: American Geophysical Union.
- Holtzman, B. K., King, D. S. H., & Kohlstedt, D. L. (2012). Effects of stress-driven melt segregation on the viscosity of rocks. *Earth and Planetary Science Letters*, 359, 184–193. <https://doi.org/10.1016/j.epsl.2012.09.030>
- Holyoke, C. W., & Tullis, J. (2006). Mechanisms of weak phase interconnection and the effects of phase strength contrast on fabric development. *Journal of Structural Geology*, 28, 621–640. <https://doi.org/10.1016/j.jsg.2006.01.008>
- Hutchinson, J. W. (1976). Bounds and self-consistent estimates for creep of polycrystalline materials. *Proceedings of the Royal Society of London. A. Mathematical and Physical Sciences*, 348, 101–127. <https://doi.org/10.1098/rspa.1976.0027>
- Jaroslow, G. E., Hirth, G., & Dick, H. J. B. (1996). Abyssal peridotite mylonites: Implications for grain-size sensitive flow and strain localization in the oceanic lithosphere. *Tectonophysics*, 256, 17–37. [https://doi.org/10.1016/0040-1951\(95\)00163-8](https://doi.org/10.1016/0040-1951(95)00163-8)
- Jessell, M. W., Bons, P. D., Griera, A., Evans, L. A., & Wilson, C. J. L. (2009). A tale of two viscosities. *Journal of Structural Geology*, 31, 719–736. <https://doi.org/10.1016/j.jsg.2009.04.010>
- Jin, D., Karato, S., & Obata, M. (1998). Mechanisms of shear localization in the continental lithosphere: Inference from the deformation microstructures of peridotites from the Ivrea zone, northwestern Italy. *Journal of Structural Geology*, 20, 195–209. [https://doi.org/10.1016/S0191-8141\(97\)00059-X](https://doi.org/10.1016/S0191-8141(97)00059-X)
- Kenkmann, T., & Dresen, G. (2002). Dislocation microstructure and phase distribution in a lower crustal shear zone—An example from the Ivrea-Zone, Italy. *International Journal of Earth Sciences*, 91(3), 445–458. <https://doi.org/10.1007/s00531-001-0236-9>
- Kilian, R., Heilbronner, R., & Stünitz, H. (2011). Quartz grain size reduction in a granitoid rock and the transition from dislocation to diffusion creep. *Journal of Structural Geology*, 33, 1265–1284. <https://doi.org/10.1016/j.jsg.2011.05.004>
- Kohlstedt, D. L. (2002). Partial melting and deformation. *Reviews in Mineralogy and Geochemistry*, 51, 121–135. <https://doi.org/10.2138/gsrng.51.1.121>
- Kohlstedt, D. L., Evans, B., & Mackwell, S. J. (1995). Strength of the lithosphere: constraints imposed by laboratory experiments. *Journal of Geophysical Research*, 100. <https://doi.org/10.1029/95jb01460>
- Kronenberg, A. K., Segall, P., & Wolf, G. H. (1990). Hydrolytic weakening and penetrative deformation within a natural shear zone. *Geophysical Monograph*, 56, 21–36.
- Kruse, R., & Stünitz, H. (1999). Deformation mechanisms and phase distribution in mafic high-temperature mylonites from the Jotun Nappe, southern Norway. *Tectonophysics*, 303, 223–249. [https://doi.org/10.1016/S0040-1951\(98\)00255-8](https://doi.org/10.1016/S0040-1951(98)00255-8)
- Linckens, J., Bruijn, R. H. C., & Skemer, P. (2014). Dynamic recrystallization and phase mixing in experimentally deformed peridotite. *Earth and Planetary Science Letters*, 388, 134–142. <https://doi.org/10.1016/j.epsl.2013.11.037>
- Linckens, J., Herwegh, M., & Müntener, O. (2015). Small quantity but large effect—How minor phases control strain localization in upper mantle shear zones. *Tectonophysics*, 643, 26–43. <https://doi.org/10.1016/j.tecto.2014.12.008>
- Lopez-Sanchez, M. A., & Llana-Fúnez, S. (2018). A cavitation-seal mechanism for ultramylonite formation in quartzofeldspathic rocks within the semi-brittle field (Vivero fault, NW Spain). *Tectonophysics*, 745, 132–153. <https://doi.org/10.1016/J.TECTO.2018.07.026>
- Mansard, N., Stünitz, H., Raimbourg, H., & Précigout, J. (2020). The role of deformation-reaction interactions to localize strain in poly-mineralic rocks: Insights from experimentally deformed plagioclase-pyroxene assemblages. *Journal of Structural Geology*, 134, 104,008. <https://doi.org/10.1016/j.jsg.2020.104008>
- Marti, S., Stünitz, H., Heilbronner, R., Plümper, O., & Kilian, R. (2018). Syn-kinematic hydration reactions, grain size reduction, and dissolution-precipitation creep in experimentally deformed plagioclase-pyroxene mixtures. *Solid Earth*, 9, 985–1009. <https://doi.org/10.5194/se-9-985-2018>
- Mehl, L., & Hirth, G. (2008). Plagioclase preferred orientation in layered mylonites: Evaluation of flow laws for the lower crust. *Journal of Geophysical Research*, 113, B05202. <https://doi.org/10.1029/2007JB005075>
- Menegon, L., Fusses, F., Stünitz, H., & Xiao, X. (2015). Creep cavitation bands control porosity and fluid flow in lower crustal shear zones. *Geology*, 43(3), 227–230. <https://doi.org/10.1130/G36307.1>
- Mulyukova, E., & Bercovici, D. (2019). The generation of plate tectonics from grains to global scales: A brief review. *Tectonics*, 38, 4058–4076. <https://doi.org/10.1029/2018TC005447>

- Newman, J., Lamb, W. M., Drury, M. R., & Vissers, R. L. (1999). Deformation processes in a peridotite shear zone: Reaction-softening by an H<sub>2</sub>O-deficient, continuous net transfer reaction. *Tectonophysics*, 303, 193–222. [https://doi.org/10.1016/S0040-1951\(98\)00259-5](https://doi.org/10.1016/S0040-1951(98)00259-5)
- Norris, R. J., & Toy, V. G. (2014). Continental transforms: A view from the Alpine Fault. *Journal of Structural Geology*, 64, 3–31. <https://doi.org/10.1016/j.jsg.2014.03.003>
- Ohuchi, T., Kawazoe, T., Higo, Y., Funakoshi, K. I., Suzuki, A., Kikegawa, T., & Irifune, T. (2015). Dislocation-accommodated grain boundary sliding as the major deformation mechanism of olivine in the Earth's upper mantle. *Science Advances*, 1. <https://doi.org/10.1126/sciadv.1500360>
- Paterson, M. S. (2007). Localization in rate-dependent shearing deformation, with application to torsion testing. *Tectonophysics*, 445, 273–280. <https://doi.org/10.1016/j.tecto.2007.08.015>
- Paterson, M. S., & Olgaard, D. L. (2000). Rock deformation tests to large shear strains in torsion. *Journal of Structural Geology*, 22, 1341–1358. [https://doi.org/10.1016/S0191-8141\(00\)00042-0](https://doi.org/10.1016/S0191-8141(00)00042-0)
- Pearce, M. A. (2015). EBSDinterp 1.0: A MATLAB program to perform microstructurally constrained interpolation of EBSD data. *Microscopy and Microanalysis*, 21(4), 985–993. <https://doi.org/10.1017/S1431927615000781>
- Pennock, G. M., Drury, M. R., & Spiers, C. J. (2005). The development of subgrain misorientations with strain in dry synthetic NaCl measured using EBSD. *Journal of Structural Geology*, 27, 2159–2170. <https://doi.org/10.1016/j.jsg.2005.06.013>
- Pieri, M., Kunze, K., Burlini, L., Stretton, I., Olgaard, D. L., Burg, J.-P., & Wenk, H.-R. (2001). Texture development of calcite by deformation and dynamic recrystallization at 1000K during torsion experiments of marble to large strains. *Tectonophysics*, 330, 119–140. [https://doi.org/10.1016/S0040-1951\(00\)00225-0](https://doi.org/10.1016/S0040-1951(00)00225-0)
- Platt, J. P. (2015). Rheology of two-phase systems: A microphysical and observational approach. *Journal of Structural Geology*, 77, 213–227. <https://doi.org/10.1016/j.jsg.2015.05.003>
- Platt, J. P., & Behrmann, J. H. (1986). Structures and fabrics in a crustal-scale shear zone, Betic Cordillera, SE Spain. *Journal of Structural Geology*, 8, 15–33. [https://doi.org/10.1016/0191-8141\(86\)90014-3](https://doi.org/10.1016/0191-8141(86)90014-3)
- Poirier, J. P. (1982). On transformation plasticity. *Journal of Geophysical Research*, 87, 6791–6797. <https://doi.org/10.1029/JB087iB08p06791>
- Pouryazdan, M., Kaus, B. J. P., Rack, A., Ershov, A., & Hahn, H. (2017). Mixing instabilities during shearing of metals. *Nature Communications*, 8(1), 1611. <https://doi.org/10.1038/s41467-017-01879-5>
- Précigout, J., Gueydan, F., Gapais, D., Garrido, C. J., & Essaifi, A. (2007). Strain localisation in the subcontinental mantle—A ductile alternative to the brittle mantle. *Tectonophysics*, 445, 318–336. <https://doi.org/10.1016/j.tecto.2007.09.002>
- Précigout, J., Prigent, C., Palasse, L., & Pochon, A. (2017). Water pumping in mantle shear zones. *Nature Communications*, 8(1). <https://doi.org/10.1038/ncomms15736>
- Précigout, J., Stünitz, H., & Villeneuve, J. (2019). Excess water storage induced by viscous strain localization during high-pressure shear experiment. *Scientific Reports*, 9(1), 1–9. <https://doi.org/10.1038/s41598-019-40020-y>
- Prior, D. J., Mariani, E., & Wheeler, J. (2009). *EBSD in the earth sciences: Applications, common practice, and challenges*. *Electron backscatter diffraction in materials science* (pp. 345–360). Boston, MA: Springer US. [https://doi.org/10.1007/978-0-387-88136-2\\_26](https://doi.org/10.1007/978-0-387-88136-2_26)
- Ramsay, J. G. (1980). Shear zone geometry: A review. *Journal of Structural Geology*, 2, 83–99. [https://doi.org/10.1016/0191-8141\(80\)90038-3](https://doi.org/10.1016/0191-8141(80)90038-3)
- Renner, J., Evans, B., & Siddiqi, G. (2002). Dislocation creep of calcite. *Journal of Geophysical Research*, 107(B12), 2364. <https://doi.org/10.1029/2001JB001680>
- Ross, J. V., & Nielsen, K. C. (1978). High-temperature flow of wet polycrystalline enstatite. *Tectonophysics*, 44, 233–261. [https://doi.org/10.1016/0040-1951\(78\)90072-0](https://doi.org/10.1016/0040-1951(78)90072-0)
- Rutter, E. H., & Brodie, K. H. (2004). Experimental grain size-sensitive flow of hot-pressed Brazilian quartz aggregates. *Journal of Structural Geology*, 26, 2011–2023. <https://doi.org/10.1016/j.jsg.2004.04.006>
- Rybacki, E., & Dresen, G. (2004). Deformation mechanism maps for feldspar rocks. *Tectonophysics*, 382, 173–187. <https://doi.org/10.1016/j.tecto.2004.01.006>
- Shinevar, W. J., Behn, M. D., & Hirth, G. (2015). Compositional dependence of lower crustal viscosity. *Geophysical Research Letters*, 42, 8333–8340. <https://doi.org/10.1002/2015GL065459>
- Skemer, P., Katayama, I., Jiang, Z., & Karato, S. (2005). The misorientation index: Development of a new method for calculating the strength of lattice-preferred orientation. *Tectonophysics*, 411, 157–167. <https://doi.org/10.1016/j.tecto.2005.08.023>
- Skemer, P., Warren, J. M., Hansen, L. N., Hirth, G., & Kelemen, P. B. (2013). The influence of water and LPO on the initiation and evolution of mantle shear zones. *Earth and Planetary Science Letters*, 375, 222–233. <https://doi.org/10.1016/j.epsl.2013.05.034>
- Skemer, P., Warren, J. M., Kelemen, P. B., & Hirth, G. (2010). Microstructural and rheological evolution of a mantle shear zone. *Journal of Petrology*, 51, 43–53. <https://doi.org/10.1093/petrology/egp057>
- Smith, C. S. (1948). Grains, Phases and interfaces: An interpretation of microstructure. *Transactions of AIME*, 175, 15–51.
- Stenvall, C. A., Fagereng, Å., & Diener, J. F. A. (2019). Weaker than weakest: On the strength of shear zones. *Geophysical Research Letters*, 46, 7404–7413. <https://doi.org/10.1029/2019GL083388>
- Stevens, R. N. (1971). Grain-boundary sliding and diffusion creep in polycrystalline solids. *Philosophical Magazine*, 23, 265–283. <https://doi.org/10.1080/14786437108216383>
- Sundberg, M., & Cooper, R. F. (2008). Crystallographic preferred orientation produced by diffusional creep of harzburgite: Effects of chemical interactions among phases during plastic flow. *Journal of Geophysical Research*, 113, B12208. <https://doi.org/10.1029/2008JB005618>
- Takeda, Y. T., & Griera, A. (2006). Rheological and kinematical responses to flow of two-phase rocks. *Tectonophysics*, 427, 95–113. <https://doi.org/10.1016/j.tecto.2006.03.050>
- Tasaka, M., Zimmerman, M. E., Kohlstedt, D. L., Stünitz, H., & Heilbronner, R. (2017). Rheological weakening of olivine + orthopyroxene aggregates due to phase mixing: Part 2. Microstructural Development. *Journal of Geophysical Research: Solid Earth*, 122, 7597–7612. <https://doi.org/10.1002/2017JB014311>
- Tokle, L., Hirth, G., & Behr, W. M. (2019). Flow laws and fabric transitions in wet quartzite. *Earth and Planetary Science Letters*, 505, 152–161. <https://doi.org/10.1016/j.epsl.2018.10.017>
- Urai, J. L., Means, W. D., & Lister, G. S. (1986). In B. E. Hobbs, & H. C. Heard (Eds.), *Dynamic recrystallization of minerals: Laboratory Studies*, *Geophysical Monograph Series*, (36, pp. 161–199). Washington, D. C: American Geophysical Union. <https://doi.org/10.1029/GM036p0161>
- Viegas, G., Menegon, L., & Archanjo, C. (2016). Brittle grain-size reduction of feldspar, phase mixing and strain localization in granitoids at mid-crustal conditions (Pernambuco shear zone, NE Brazil). *Solid Earth*, 7, 375–396. <https://doi.org/10.5194/se-7-375-2016>

- Warren, J. M., & Hirth, G. (2006). Grain size sensitive deformation mechanisms in naturally deformed peridotites. *Earth and Planetary Science Letters*, 248, 438–450. <https://doi.org/10.1016/j.epsl.2006.06.006>
- White, S. H. (1976). The effects of strain on the microstructures, fabrics, and deformation mechanisms in quartzites. *Philosophical Transactions of the Royal Society of London A*, 283, 69–86.
- White, S. H., Burrows, S. E., Carreras, J., Shaw, N. D., & Humphreys, F. J. (1980). On mylonites in ductile shear zones. *Journal of Structural Geology*, 2, 175–187.
- White, S. H., & Knipe, R. J. (1978). Transformation- and reaction-enhanced ductility in rocks. *Journal of the Geological Society*, 135, 513–516. <https://doi.org/10.1144/gsjgs.135.5.0513>
- Wiesman, H. S., Zimmerman, M. E., & Kohlstedt, D. L. (2018). Laboratory investigation of mechanisms for phase mixing in olivine + ferropericlasite aggregates. *Philosophical Transactions of the Royal Society A - Mathematical Physical and Engineering Sciences*, 376, 20170417. <https://doi.org/10.1098/rsta.2017.0417>
- Zhang, G., Mei, S., Song, M., & Kohlstedt, D. L. (2017). Diffusion creep of Enstatite at high pressures under hydrous conditions. *Journal of Geophysical Research: Solid Earth*, 122, 7718–7728. <https://doi.org/10.1002/2017JB014400>
- Zhang, Y., Hobbs, B. E., & Jessell, M. W. (1994). The effect of grain-boundary sliding on fabric development in polycrystalline aggregates. *Journal of Structural Geology*, 16, 1315–1325. [https://doi.org/10.1016/0191-8141\(94\)90072-8](https://doi.org/10.1016/0191-8141(94)90072-8)
- Zhao, N., Hirth, G., Cooper, R. F., Kruckenberg, S. C., & Cukjati, J. (2019). Low viscosity of mantle rocks linked to phase boundary sliding. *Earth and Planetary Science Letters*, 517, 83–94. <https://doi.org/10.1016/j.epsl.2019.04.019>

## Erratum

The originally published version of this article contained an error resulting from the miscalculation of one parameter used to construct contour maps in Figure 9. The error did not affect the scientific results or text of the article. Figure 9 has been corrected, and this may be considered the official version of record.